EXPERIMENTAL PLASMA EQUILIBRIUM RECONSTRUCTION FROM KINETIC AND MAGNETIC MEASUREMENTS IN THE FTU TOKAMAK

F. ALLADIO, P. MICOZZI
Associazione Euratom–ENEA sulla Fusione,
Centro Ricerche Energia Frascati,
Frascati (Rome), Italy

ABSTRACT. The behaviour of the FTU tokamak plasma has been analysed by using two reconstructive MHD equilibrium codes: the first code works by using the magnetic data alone and the second one by including as well the shape of the kinetic pressure profile, as obtained from the measured profiles of electron temperature T_e and density n_e. The code that analyses the magnetic data alone provides a good evaluation of the macroscopic quantities such as the poloidal beta β_p and the internal inductance l_i, if the plasma elongation is greater than 1.04. No detailed information about the toroidal current density profile J_ϕ and the safety factor profile q can be obtained from the magnetic data alone. On the other hand, the coupling of magnetic and kinetic data is able to provide a reasonable estimate of the toroidal current density profile and of its behaviour during the plasma discharge. The reliability of the J_ϕ and q profile reconstruction has been explored and validated by a detailed comparison with the observed MHD behaviour of the FTU plasma discharges. A good agreement between the appearance of the sawtooth activity and the drop of the safety factor on the magnetic axis q_0 to unity is observed. Also, at least for edge safety factors q_ψ less than 4, the sawtooth inversion radius is found to be very close to the $q = 1$ surface. A remarkable correspondence between J_ϕ and $T_e^{3/2}$ is found in sawtoothing discharges. The structure of the snake oscillation in pellet injected discharges is found to be strictly correlated to the position of the $q = 1$ surface. A cylindrical linear tearing mode stability calculation applied to the reconstructed J_ϕ profile has shown qualitative agreement with the appearance of the Mirnov oscillations. Finally, the magnetic reconnections between double resonant surfaces during the rise of the plasma current or after the pellet injection have provided an interesting validation of the J_ϕ profile reconstruction.

1. INTRODUCTION

Knowledge of the toroidal plasma current density profile J_ϕ and of its time evolution during a plasma discharge is one of the most important pieces of information that is required from any tokamak experiment.

It is well known [1–4] that the magnetic measurements alone are able to provide an evaluation of integral plasma quantities such as the poloidal beta β_p and the internal inductance l_i, provided that the toroidicity and the shaping of the plasma column are strong enough to remove the cylindrical degeneracy. On the contrary, the magnetic data alone are not sufficient to give detailed information about the profile of the toroidal current density J_ϕ [1, 5].

The most investigated approach [5, 6] in order to overcome this limitation is to couple in the same equilibrium code the data obtained from the magnetic sensors with those derived from other diagnostics, such as the ECE measurements that provide the electron temperature profile T_e, the interferometric measurements of the electron density profile n_e, the Thomson scattering that provides both T_e and n_e, the active charge exchange diagnostics that provide the ion temperature profile T_i, the shape of the internal flux surfaces as measured by a soft X ray pinhole camera [7], the Faraday effect polarimetry [8–11], the motional Stark effect measurements [12–15] and the Zeeman effect spectroscopy [16–18] that provide more or less direct measurements of the poloidal magnetic field. At the moment, in the case of the FTU experiment [19] only the first step of coupling the magnetic data to the electron temperature and density profiles has been undertaken.

The structure of the paper is the following.

In Section 2 a short description of the purely magnetic reconstructive equilibrium code ODIN is given, together with the results of its application to the FTU discharges, and the determination of the integral plasma quantities is discussed.

Section 3 is devoted to a description of the code ODINP that couples the magnetic data with the shape of the electron pressure profile as obtained from the ECE and DCN interferometer diagnostics.

In Section 4 the current density J_ϕ and the safety factor q profiles provided by the code ODINP are compared in detail with the experimental behaviour of the MHD instabilities of the FTU plasmas.

Finally, Section 5 is devoted to the conclusions.

2. THE UNCONDITIONED RECONSTRUCTIVE MHD EQUILIBRIUM CODE (ODIN)

The magnetic data of the FTU machine are elaborated by the reconstructive MHD equilibrium code ODIN; the equilibrium solution procedures and algorithms have been fully sketched in Ref. [1], where an application to the JET tokamak was also presented.

The source of the Grad–Shafranov equation [20] is, in cylindrical co-ordinates $(R,\ Z,\ \phi)$:

$$J_\phi(R,\ \psi) = 2\pi R\frac{\mathrm{d}P(\psi)}{\mathrm{d}\psi} + \frac{\mu_0}{4\pi R}\frac{\mathrm{d}F^2(\psi)}{\mathrm{d}\psi} \tag{1}$$

The functional forms for the pressure P and for the diamagnetic current F are assumed to be

$$P(\psi) = p_\alpha\psi^\alpha + p_\beta\psi^\beta \tag{2a}$$

$$F^2(\psi) = f_\alpha\psi^\alpha + f_\beta\psi^\beta \tag{2b}$$

The poloidal flux function $\psi = 2\pi RA_\phi$ ($\boldsymbol{A}$ being the magnetic vector potential) is chosen in the range $[0, \psi_{\max}]$, with $\psi = 0$ at the plasma boundary and $\psi = \psi_{\max}$ at the magnetic axis. The safety factor q is defined as $\mathrm{d}\Phi/\mathrm{d}\psi$, where in the toroidal flux $\Phi(\psi)$ the contribution of the diamagnetic current $F(\psi)$ is included.

One of the most suitable methods of solving the equilibrium problem is the use of a multipolar expansion in particular geometries. In this paper ψ is expanded [1] in a series of toroidal multipoles, by using the fully toroidal co-ordinate system $(\vartheta,\ \overline{\omega},\ \phi)$ [21], in the form

$$\begin{aligned}\psi = \frac{1}{\sqrt{\cosh\vartheta - \cos\overline{\omega}}}\sum_{m=0}^{m_{\max}}\{&[M_m^{\mathrm{i,c}}(\vartheta)f_m(\cosh\vartheta)\\ &+ M_m^{\mathrm{e,c}}(\vartheta)g_m(\cosh\vartheta)]\cos(m\overline{\omega})\\ &+ [M_m^{\mathrm{i,s}}(\vartheta)f_m(\cosh\vartheta)\\ &+ M_m^{\mathrm{e,s}}(\vartheta)g_m(\cosh\vartheta)]\sin(m\overline{\omega})\}\end{aligned} \tag{3}$$

where $M_m^{\mathrm{i,c/s}}$ and $M_m^{\mathrm{e,c/s}}$ are the (cosine/sine symmetric) toroidal multipolar internal and external moments and $f_m(\cosh\vartheta)$ and $g_m(\cosh\vartheta)$ are the Fock functions [22].

The toroidal moment expansion outside the plasma is obtained from the fluxes and fields measured by the magnetic diagnostics of FTU and represents the boundary condition of the problem. The number of harmonics $m_{\max}$, at which the series of Eq. (3) is truncated, is determined [1] by the error bars on the magnetic measurements. The magnetic diagnostics assembly of the FTU tokamak and the uncertainties on the magnetic measurements are discussed in detail in Appendix A. The main systematic error that affects the magnetic measurements is the spurious pick-up of the toroidal field B_T, due to misalignments of the sensors and to the time evolution of the ripple field components. In order to remove this error, one has to subtract the signal of a purely toroidal field reference shot; this reference shot is usually produced any time the waveform of the toroidal magnet current is changed or it is updated on a daily basis. As a result the time behaviour of the first four toroidal multipolar moments, from $m = 0$ to $m = 3$, is accurately measured on FTU, with a sampling of 2 ms and an inaccuracy in the plasma boundary position of less than $\pm 1\%$ of the minor radius of the discharge and an uncertainty of $\pm 1\%$ in the value of the poloidal field B_{pol} at the plasma boundary.

The coefficients p_α, p_β, f_α and f_β of Eq. (2) are iteratively readjusted [1], during the solution procedure, in order to fit the first four internal (cosine symmetric) moments $M_m^{\mathrm{i,c}}$ of the multipolar expansion outside the plasma. The iterative solution algorithm computes, with a sampling of 20 ms, the radial behaviour of the multipolar moments. The iteration is started from the equilibrium solution already obtained at a neighbouring time slice or from a guessed ψ function and from a reasonable choice of the coefficients p_α, p_β, f_α and f_β for the first time slice. The renormalization of the internal sine symmetric moments $M_m^{\mathrm{i,s}}$ during the iterations is simply obtained, step by step, by forcing their values outside the plasma to be equal to the measured ones, after the readjustment of the cosine symmetric part.

The sum $\beta_\mathrm{p} + l_\mathrm{i}/2$ can be derived directly from the magnetic measurements by computing the Shafranov integrals [23]. In Ref. [1] a detailed investigation about the separability of $\beta_\mathrm{p} + l_\mathrm{i}/2$ was carried out by solving the equilibrium equation. The conclusion was that it is possible to obtain the separate values of β_p and l_i in all the situations in which there is a sensible detachment between the flux surfaces and the constant J_ϕ surfaces, so that high elongation, high values of $\beta_\mathrm{p} + l_\mathrm{i}/2$ and low aspect ratios are favourable for this aim. The analysis of Ref. [1] shows that, for the FTU aspect ratio ($R/a = 3.16$), assuming a random error in the magnetic measurements of the order of $\pm 1\%$, there is a threshold of about 1.25 in the value of $\beta_p + l_i/2$ in order to obtain the separation for a circular cross-section plasma. Such a threshold is strongly lowered by increasing the plasma elongation.

This conclusion has been widely confirmed by the analysis of the experimental data of the FTU tokamak. For plasma elongations k greater than 1.04, the sensitivity of the separation of β_p and l_i performed by the code ODIN, as a function of the variation of the exponents α, β in Eq. (2), is shown in Figs 1 to 3. The largest possible range for the values of α and β has been selected for each shot using as a constraint that both the toroidal current density J_ϕ, as well as the plasma pressure $P(\psi)$, must not become negative on the magnetic axis. The fit to the magnetic data is independent of the choices of α and β, as detailed in Appendix A.

Figure 1 deals with the time behaviour of β_p and l_i for shot No. 2728 ($B_T = 6$ T, $I_p = 350$ kA, $q_\psi = 7.8$). For such a high q_ψ shot it is possible to have a broad range of variation (1.3 to 3.5) for α and β. Consequently the error bars on the separation of β_p and l_i are quite relevant: $\Delta\beta_p/\beta_p = 50\%$ and $\Delta l_i/l_i = 12\%$.

Figure 2 shows the time behaviour of β_p and l_i for shot No. 4023 ($B_T = 6$ T, $I_p = 850$ kA, $q_\psi = 3.3$). For such a medium q_ψ shot the range of variation for α and β is more restricted (1.3 to 2.7). In this case the separation of β_p and l_i is much less uncertain ($\Delta\beta_p/\beta_p = 15\%$, $\Delta l_i/l_i = 6\%$).

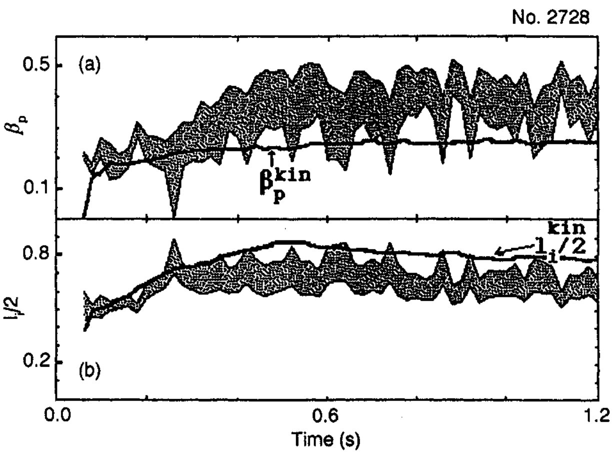

FIG. 1. Shot No. 2728 (I_p = 350 kA, B_T = 6 T, q_ψ = 7.8, $\bar{n}_e$ = (0.4–0.5) × 10^{20} m^{-3}). Wave forms of (a) poloidal beta β_p and (b) internal inductance $l_i/2$. The solid lines show the kinetic values and the shaded regions represent the error bars of the ODIN code obtained by the largest possible variation of the arbitrary exponents α and β in $P(\psi) = p_\alpha\psi^\alpha + p_\beta\psi^\beta$ and $F^2(\psi) = f_\alpha\psi^\alpha + f_\beta\psi^\beta$.

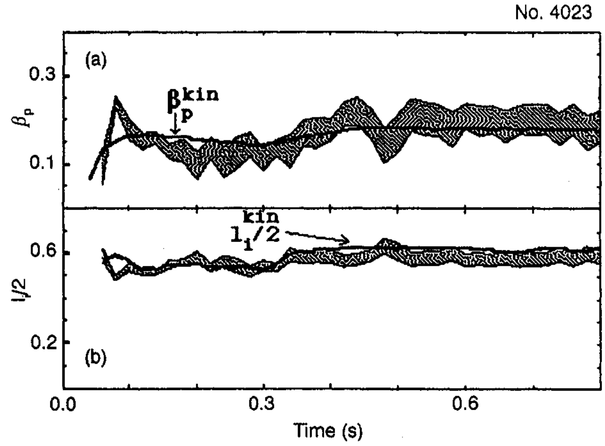

FIG. 2. Shot No. 4023 (I_p = 850 kA, B_T = 6 T, q_ψ = 3.3, $\bar{n}_e$ = (1.2–1.4) × 10^{20} m^{-3}). Wave forms of (a) poloidal beta β_p and (b) internal inductance $l_i/2$. The solid lines show the kinetic values and the shaded regions represent the error bars of the ODIN code.

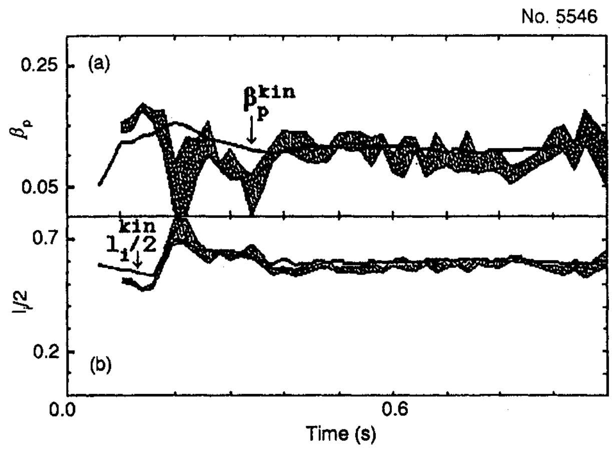

FIG. 3. Shot No. 5546 (I_p = 1.2 MA, B_T = 6 T, q_ψ = 2.5, $\bar{n}_e$ = (1.3–1.5) × 10^{20} m^{-3}). Wave forms of (a) poloidal beta β_p and (b) internal inductance $l_i/2$. The solid lines show the kinetic values and the shaded regions represent the error bars of the ODIN code.

Figure 3 deals with the time behaviour of β_p and l_i for shot No. 5546 ($B_T = 6$ T, $I_p = 1.2$ MA, $q_\psi = 2.5$). For such a low q_ψ shot the range of variation for α and β is much more restricted (1.3 to 1.8). In this case the separation of β_p and l_i is even less uncertain ($\Delta\beta_p/\beta_p = 12\%$, $\Delta l_i/l_i = 5\%$).

On the basis of the previous results, the intermediate values $\alpha = 1.5$ and $\beta = 2.5$ have been chosen, for the sake of uniformity, in the analysis of all the shots of FTU. Nevertheless, in the low q_ψ cases ($q_\psi < 3$) this choice may not be the best one.

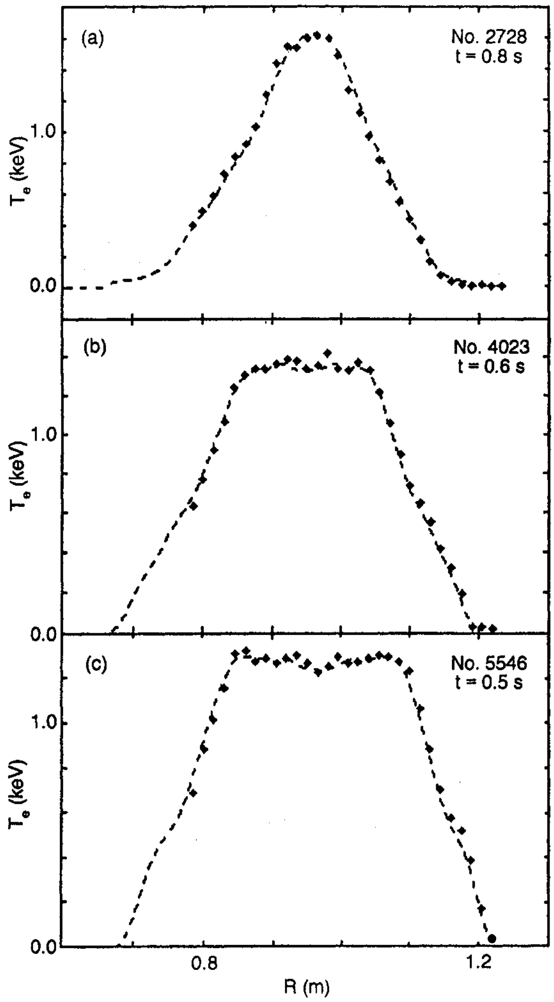

FIG. 4. Radial profiles (on the midplane Z = 0) of the electron temperature T_e. The crosses represent the ECE data, the dotted lines come from the symmetrization of the T_e profile with respect to the flux function ψ computed by the ODIN code: (a) shot No. 2728 at t = 0.8 s; (b) shot No. 4023 at t = 0.6 s; (c) shot No. 5546 at t = 0.5 s.

In order to check the absolute values of β_p and l_i, as obtained by the purely magnetic code, an evaluation of the kinetic poloidal beta β_p^{kin} has been performed. The radial profile of the electron temperature T_e is obtained from ECE measurements [24]. Figure 4 shows that $T_e = T_e(\psi)$ is well verified (also the radial position of the plasma magnetic axis is in good agreement with the weight centre of the ECE temperature profile). A linear extrapolation to $T_e(\psi_{max})$ is necessary if the plasma has a considerable vertical shift with respect to the line of sight of the ECE diagnostics, which looks on the FTU midplane ($Z = 0$), from $R = 0.785$ m to the outer limiter position. The plasma density profile is computed using the data coming from a five channel DCN interferometer [25]. Such a diagnostic measures the line integral of the plasma density, and the spatial profiles of the electron density are obtained by means of a Zernicke inversion [26–28] based on the assumption that

$$n_e(\psi) = n_0 + n_1\psi^{1/2} + n_2\psi + n_3\psi^{3/2} \tag{4}$$

where the flux function ψ is that obtained from the equilibrium code ODIN and the coefficients n_0, n_1, n_2 and n_3 are best-fit parameters. A detailed description of the inversion procedure is given in Appendix B.

Knowledge of $T_e(\psi)$ and $n_e(\psi)$ allows for the computation of the electron poloidal beta, $\beta_{p,e}$, through the electron pressure integral

$$\int_0^{\psi_{max}} n_e(\psi)T_e(\psi)\frac{dV}{d\psi}d\psi \tag{5}$$

in which the ψ derivative of the plasma volume $dV/d\psi$ comes from the ODIN equilibrium solution.

Assuming that the electron and ion poloidal betas are almost equal ($\beta_{p,i} \approx \beta_{p,e}$), one can define the kinetic poloidal beta as $\beta_p^{kin} = 2\beta_{p,e}$. This assumption, which is fully justified only when the ion and electron temperatures are equal ($T_i = T_e$) and when the ion and electron densities the same ($n_i = n_e$), i.e. in high density pure hydrogen plasmas with $Z_{eff} = 1$,

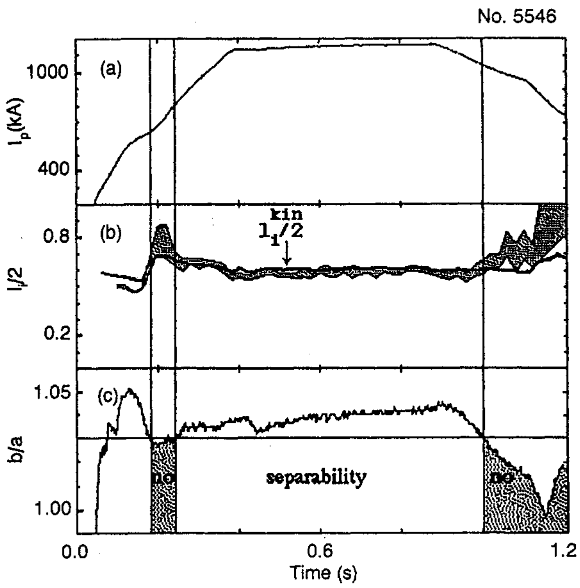

FIG. 5. Shot No. 5546. Wave forms of (a) plasma current I_p, (b) internal inductance $l_i/2$ (the solid line is the kinetic value, the shaded region shows the error bar of the ODIN code) and (c) plasma elongation b/a (the time domains where separation is not possible are shaded).

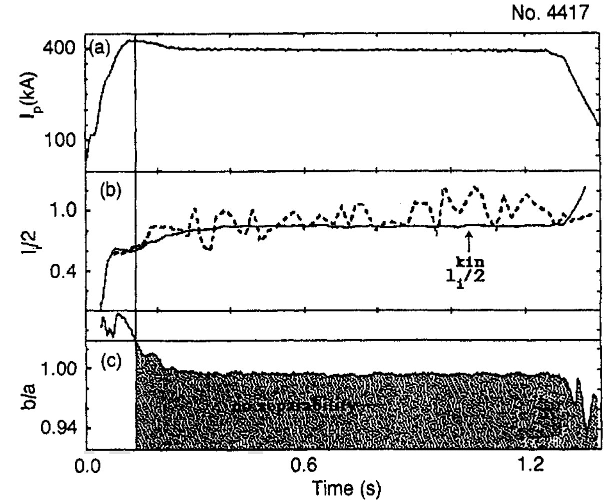

FIG. 6. Shot No. 4417 (B_T = 6 T, $\overline{n}_e = 0.4 \times 10^{20}$ m^{-3}). Wave forms of (a) plasma current I_p, (b) internal inductance $l_i/2$ (the solid line is the kinetic value, the dotted one comes from the ODIN code) and (c) plasma elongation b/a (the time domain where separation is not possible is shaded).

remains a good approximation for densities down to $\overline{n}_e \approx 4\times10^{19}$ m^{-3}, as the ion pressure profile becomes lower in the centre but broader in radial width than the electron pressure profile.

A kinetic value for the internal inductance can also be deduced by subtracting this β_p^{kin} from the sum $\beta_p + l_i/2$ coming from the magnetic data, i.e. $l_i^{kin}/2 = (\beta_p + l_i/2)^{eq} - \beta_p^{kin}$.

In all the cases in which the plasma elongation is not sufficient ($k < 1.04$), it is impossible to achieve a good separation between β_p and l_i. This is detailed in Fig. 5 for the case of shot No. 5546 in which the elongation decays after $t = 1.0$ s: after this time the internal magnetic inductance goes wrong with respect to the kinetic one. The same point is further substantiated in Fig. 6 for the case of shot No. 4417, in which a perfectly circular cross-section plasma exhibits an enormous separation noise for the internal magnetic inductance, corresponding to a 100% uncertainty in β_p^{eq}.

However, there are other circumstances in which the separation does not work correctly. First of all, the comparison with β_p^{kin} and l_i^{kin} is not correct if the electron density is too low ($\overline{n}_e < 4\times10^{19}$ m^{-3}), because in this case T_i becomes much lower than T_e and n_i, much lower than n_e, due to the increased Z_{eff}, and the larger width of the ion pressure profile is no longer able to make $\beta_{p,i} = \beta_{p,e}$. So β_p^{kin} is significantly lower than $2\beta_{p,e}$ and the discrepancy is not due to a deficiency of the reconstructive code but only to an incorrect evaluation of the kinetic data.

On the contrary, real discrepancies arise during strong transients of the plasma current, as in the early phase of the ramp-up or in pulses with two levels of plasma current, such as shot No. 3882, where I_p decreases from 0.90 to 0.45 MA in 60 ms (see Fig. 7). This problem is due to the positioning of the magnetic sensors on the FTU tokamak (see Fig. 28). In fact they are located externally to the vacuum vessel of the machine, so the vessel currents are seen as a spurious contribution to the plasma current and the computed values of the internal multipolar moments are not correct in this case.

A different behaviour is observed during the discharges characterized by a plasma detachment phenomenon [29], which is observed at high q_ψ, high n_e and in the presence of low Z impurities, as shown in Fig. 8 for shot No. 2461 (B_T = 6 T, I_p = 350 kA). In this case the value of β_p^{eq} is higher than the kinetic value β_p^{kin} and this discrepancy is not compensated even by the broad range of variation (1.3–3.5) for the exponents α and β that is allowed at high q_ψ values. A possible explanation could be linked to the plasma rotation that may be present during this phenomenon, as indicated by the fast toroidal rotation (15–25 kHz) of the MHD activity in detached plasmas. In this case

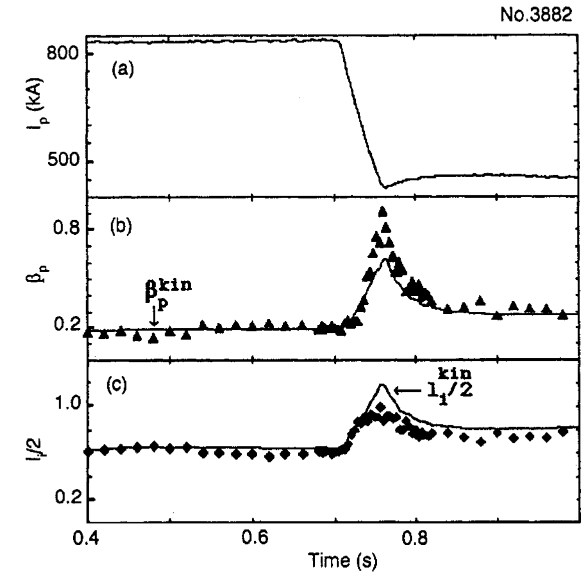

FIG. 7. Shot No. 3882 (B_T = 6 T, $\overline{n}_e$ = (1.1–0.9) $\times 10^{20}$ m^{-3}). Wave forms of (a) plasma current I_p (showing the current ramp-down from 0.9 to 0.45 MA in 60 ms), (b) poloidal beta β_p and (c) internal inductance $l_i/2$. For (b) and (c) the solid lines show the kinetic values and the triangles and diamonds represent the ODIN code results.

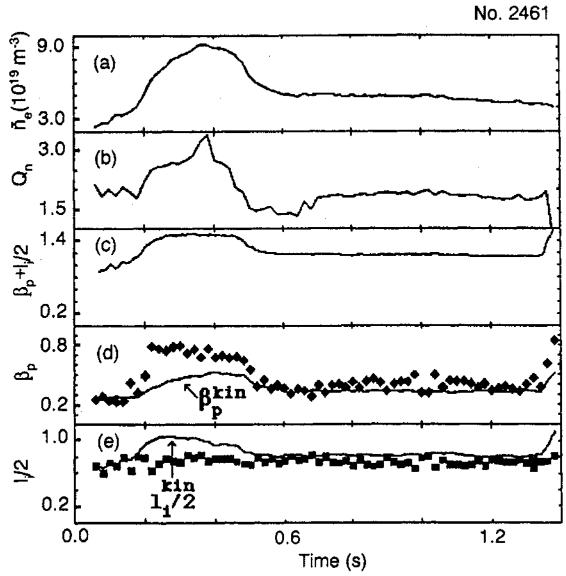

FIG. 8. Shot No. 2461 ($I_p = 350$ kA, $B_T = 6$ T). Wave forms of (a) line integrated density $\bar{n}_e$ through the plasma axis from the DCN interferometer, (b) peaking of the density profile ($Q_n = n_{e,axis}/\langle n_e \rangle_{vol}$), (c) $\beta_p + l_i/2$ from the magnetic measurements, (d) poloidal beta β_p and (e) internal inductance $l_i/2$. For (d) and (e) the solid lines are the kinetic values and the diamonds and squares represent the ODIN code results.

the assumptions that are at the basis of the Grad–Shafranov equation are not satisfied.

Some discrepancies, or absence of equilibrium convergence, are also observed in the presence of quasi-stationary modes (QSM) [30], that break the toroidal symmetry of the plasma column, as in shot No. 3971 with $I_p = 700$ kA (see Fig. 9A). The correspondence between β_p^{eq} and β_p^{kin}, in the presence of a QSM with toroidal mode number $n = 1$, can be recovered by averaging the magnetic data coming from opposite toroidal positions (see Fig. 9B).

In Fig. 10(a) the comparison between β_p^{eq} from the unconditioned code and β_p^{kin} is shown and in Fig. 10(b) the corresponding l_i^{eq} and l_i^{kin} are compared. The used database comes from the general FTU energy confinement database of deuterium plasma at $B_T = 6$ T, updated to the summer of 1993 [31]. The selection criteria for obtaining the confinement database, which is composed of 454 points from all the shots of FTU, have been the presence of sawtooth activity and the quasi-steady-state condition of the discharge at the selected time. The dataset shown in Fig 10 is further restricted to 387 points, where the 67 discarded points have been excluded for the following reasons: 5 shots for minor problems, 7 shots for not having enough elongation ($b/a < 1.04$), 10 shots for being strongly detached plasmas and 45 shots for which the purely toroidal field reference shot is not adequate and gives a systematic offset to the data.

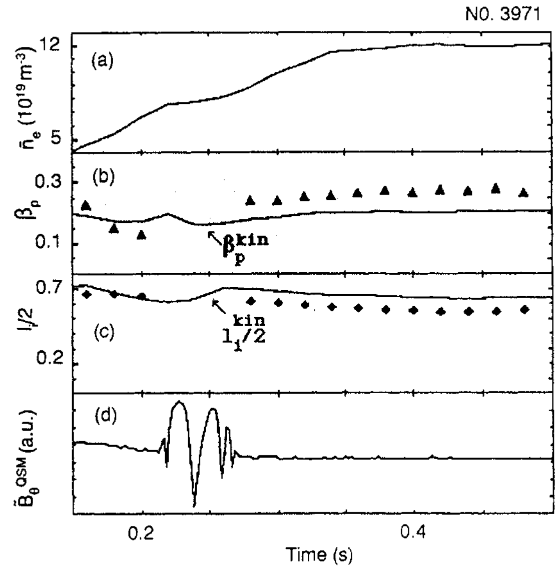

FIG. 9A. Shot No. 3971 ($I_p = 700$ kA, $B_T = 6$ T). Wave forms of (a) line integrated density $\bar{n}_e$ through the plasma axis from the DCN interferometer, (b) poloidal beta β_p, (c) internal inductance $l_i/2$ and (d) n = 1 component of the radial magnetic field (derived from two opposite toroidal positions) showing the appearance of a QSM. For (b) and (c) the solid lines are the kinetic values and the triangles and diamonds represent the ODIN code results. There is no equilibrium convergence during the QSM period.

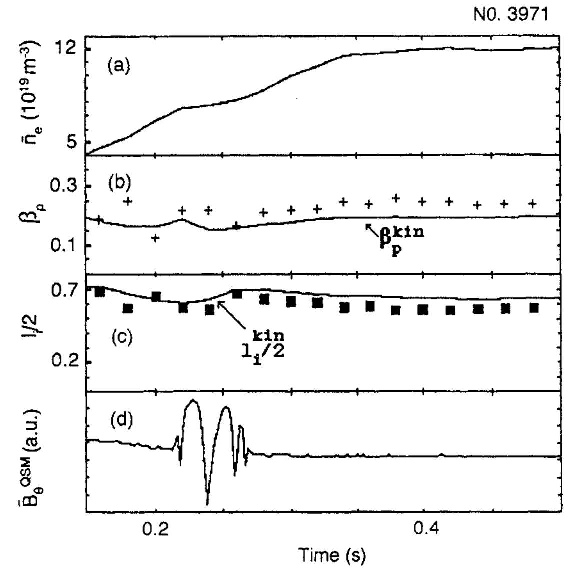

FIG. 9B. The same quantities as in Fig. 9A. The equilibrium reconstruction is performed, in this case, by averaging the magnetic data coming from opposite toroidal positions. The convergence of the ODIN code is also obtained during the OSM.

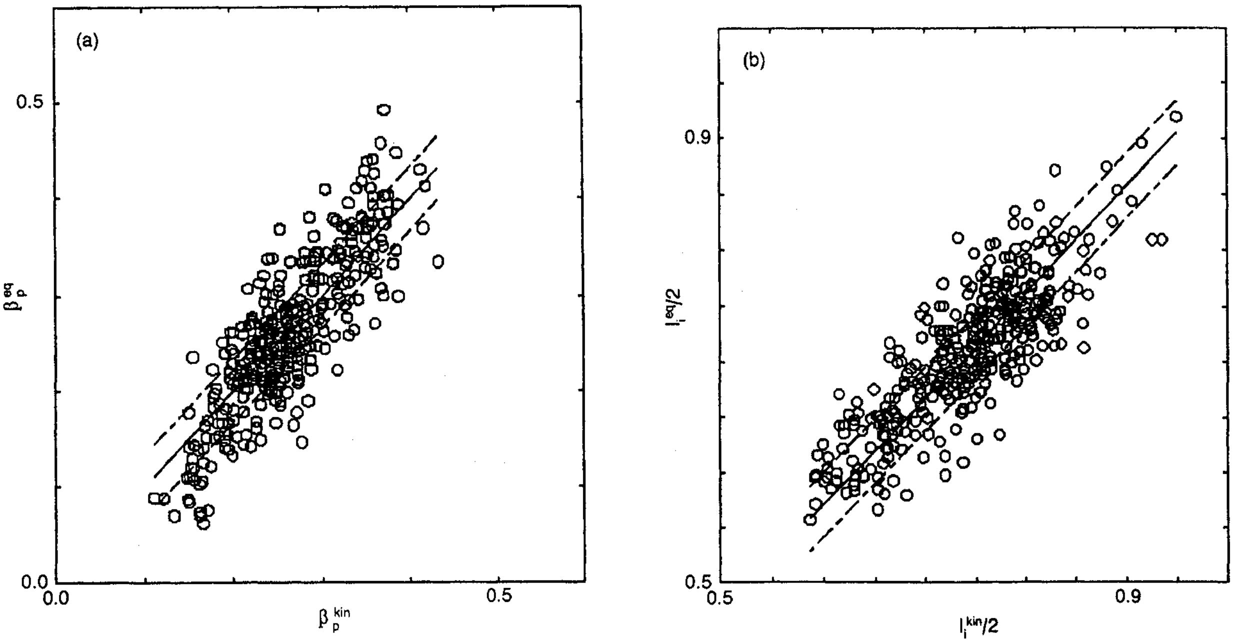

FIG. 10. (a) Comparison between β_p^{eq} from the unconditioned ODIN code and β_p^{kin} and (b) comparison between $l_i^{eq}/2$ from the ODIN code and $l_i^{kin}/2$. The database used comes from the general FTU energy confinement database for a deuterium plasma at $B_T = 6$ T and is composed of 387 points. The least squares fit coefficient (full line) in (a) is $\beta_p^{eq} = 0.99\beta_p^{kin}$, with a standard deviation of $\Delta\beta_p = 0.03$ (dashed lines). The least squares fit coefficient (full line) in (b) is $l_i^{eq}/2 = 0.95 l_i^{kin}/2$, with a standard deviation of $\Delta l_i/2 = 0.03$ (dashed lines).

The least squares fit coefficient in Fig. 10(a) is $\beta_p^{eq} = 0.99\beta_p^{kin}$, with a standard deviation of $\Delta\beta_p = 0.03$, which means a spread of $\pm30\%$ at low β_p, which is reduced to $\pm7\%$ at high β_p. The least squares fit coefficient in Fig. 10(b) is $l_i^{eq}/2 = 0.95\, l_i^{kin}/2$, with a standard deviation of $\Delta l_i/2 = 0.03$, which means a spread of $\pm5\%$ at low $l_i/2$ which is reduced to $\pm3\%$ at high l_i.

3. THE CONDITIONED RECONSTRUCTIVE MHD EQUILIBRIUM CODE (ODINP)

The reasonable agreement between the kinetic and magnetic evaluations of the poloidal beta suggests that an improved equilibrium code (ODINP) can be obtained by using the real functional form of the measured electron plasma pressure instead of the parametrization of Eq. (2).

Making the assumption that the shape of the plasma pressure profile is the same as the shape of the measured electron pressure profile (i.e. $p(\psi)/p_{max} = p_e(\psi)/p_{emax}$), the new P and F functions are

$$P(\psi) = p_{max}\frac{n_e(\psi)T_e(\psi)}{(n_eT_e)_{max}}$$

$$F^2(\psi) = f_\alpha\psi^\alpha + f_\beta\psi^\beta + f_\gamma\psi^\gamma; \quad \text{with } \alpha < \beta < \gamma \qquad (6)$$

and the solution procedure is the same as in Ref. [1]. The fit to the magnetic data is independent from the choices of α, β and γ, as detailed in Appendix A. In this case the four coefficients that must match the internal multipolar moments are p_{max}, f_α, f_β and f_γ.

It has to be remarked that the maximum value p_{max} of the pressure profile $P(\psi)$ is an output of ODINP and cannot be fixed a priori by the kinetic data alone. The reason is that the information about the splitting of $\beta_p + l_i/2$, i.e. about the kinetic global energy content of the plasma column, is already present in the multipolar expansion of the flux function ψ. Therefore, if the kinetic poloidal beta is in agreement with the magnetic one, no improvement is obtained by fixing it to the kinetic value. On the other hand, if too large a discrepancy between β_p^{kin} and β_p^{eq} exists, the ODINP code does not converge when the P profile is forced to the value of the kinetic one.

All the data used by the ODINP code (i.e. n_e, T_e and the time behaviour of the multipolar moments) are averaged on ±10 ms to reduce the noise, so the typical time resolution of the quantities obtained by the code is 20 ms.

In Figs 11 to 13 the sensitivity of the separation of β_p and l_i performed by the conditioned ODINP code, as a function of the variation of the exponents $\alpha <$

$\beta < \gamma$ in Eq. (6), is shown; these shots are the same as those studied in Figs 1 to 3 with the unconditioned ODIN code. The largest possible range for the extreme exponents α and γ is imposed by the convergence of the code, whereas the exponent β can be chosen almost at will within the range $[\alpha, \gamma]$.

Figure 11 deals with the time behaviour of β_p, l_i and q_0 for shot No. 2728. For such a high q_ψ shot it is possible to have a broad range of variation ($\alpha = 1.5$ and $\gamma = 5$). Moving the exponent β between 2 and 4.5 gives the largest possible variation for all the quantities. The error bars on the separation of β_p and l_i are enormously reduced with respect to the unconditioned code (see Fig. 1). The value of q_0 is between 0.8 and 1.1 during the sawtoothing phase of the discharge.

Figure 12 shows the time behaviour of β_p, l_i and q_0 for shot No. 4023. For such a medium q_ψ shot the range of variation is more restricted ($\alpha = 1.5$ and $\gamma = 4.5$, with β moving from 2 to 3.5). In this case the separation of β_p and l_i is invariant with respect to the parametrization of $F^2(\psi)$. The value of q_0 is between 0.8 and 1.2 during the sawtoothing phase.

Figure 13 deals with the time behaviour of β_p, l_i and q_0 for shot No. 5546. For such a low q_ψ shot the range of variation remains $\alpha = 1.5$ and $\gamma = 4.5$, with β moving from 2 to 3.5. Also in this case the separation of β_p and l_i is invariant with respect to the parametrization of $F^2(\psi)$. The uncertainty on q_0 is between 0.8 and 1.0.

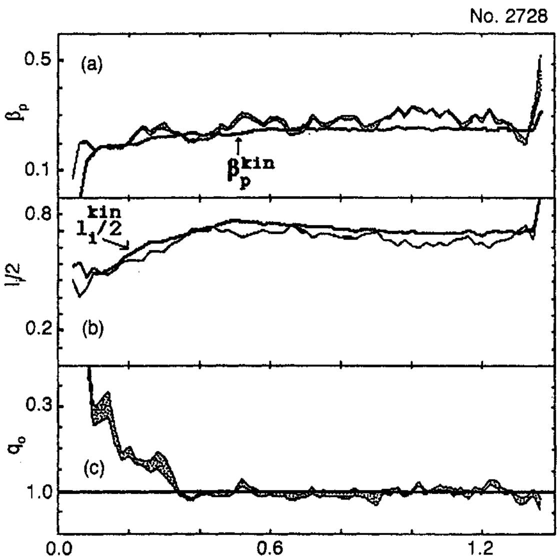

FIG. 11. Shot No. 2728. The same as Fig. 1, along with the time behaviour of q_0*, for the results of the kinetic–magnetic reconstructive equilibrium code ODINP. The solid lines show the kinetic values and the shaded regions represent the error bars of the ODINP code obtained by the largest possible variation of the arbitrary exponents* α, β *and* γ *in* $F^2(\psi) = f_\alpha\psi^\alpha + f_\beta\psi^\beta + f_\gamma\psi^\gamma$.

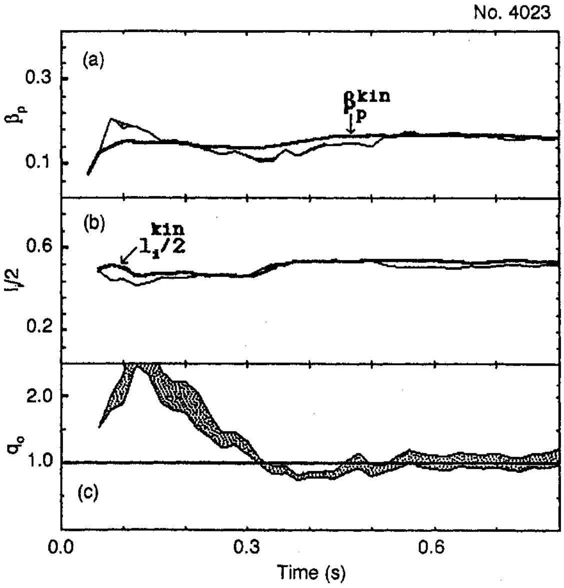

FIG. 12. Shot No. 4023. The same as Fig. 2, along with the time behaviour of q_0*, for the results of the kinetic–magnetic reconstructive equilibrium code ODINP. The solid lines show the kinetic values and the shaded regions represent the error bars of the ODINP code.*

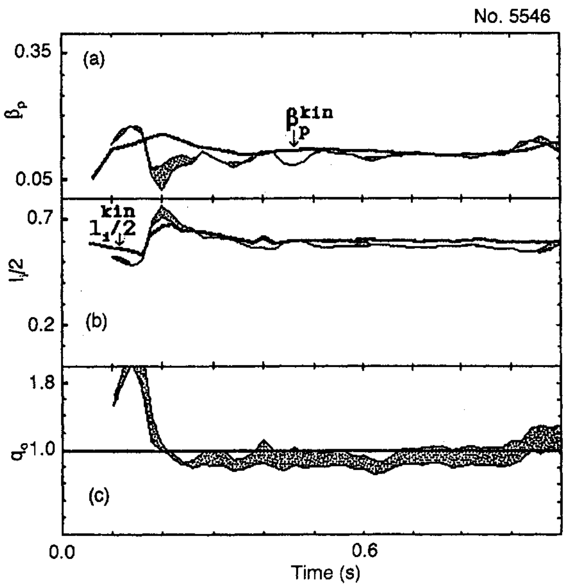

FIG. 13. Shot No. 5546. The same as Fig. 3, along with the time behaviour of q_0*, for the results of the kinetic–magnetic reconstructive equilibrium code ODINP. The solid lines show the kinetic values and the shaded regions represent the error bars of the ODINP code.*

On the basis of these results, the standard values $\alpha = 1.5$, $\beta = 2.5$ and $\gamma = 3.5$ have been chosen, for the sake of uniformity, in the analysis of all the shots of FTU.

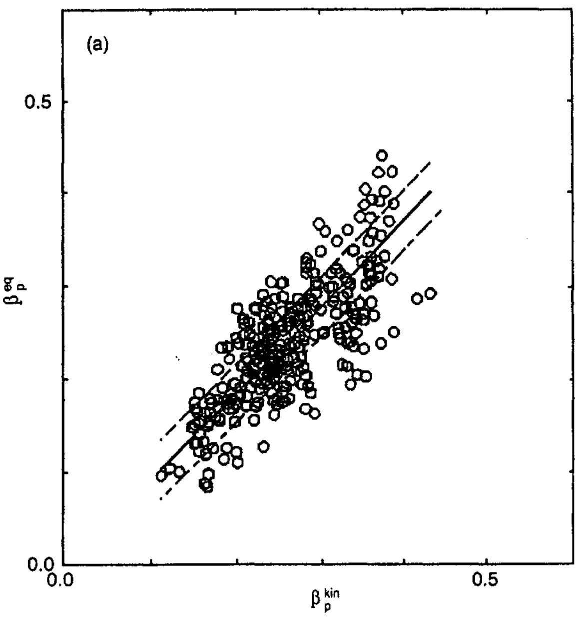

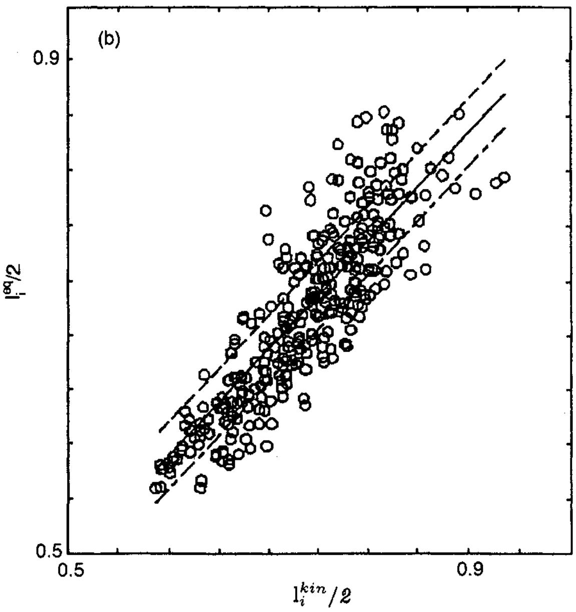

FIG. 14. (a) Comparison between β_p^{eq} from the conditioned code ODINP and β_p^{kin} and (b) comparison between $l_i^{eq}/2$ from the ODINP code and $l_i^{kin}/2$. The database used comes from the general FTU energy confinement database for a deuterium plasma at $B_T = 6$ T and is composed of 342 points. The least squares fit coefficient in (a) is $\beta_p^{eq} = 0.91\beta_p^{kin}$, with a standard deviation of $\Delta\beta_p = 0.03$. The least squares fit coefficient in (b) is $l_i^{eq}/2 = 0.98 l_i^{kin}/2$, with a standard deviation of $\Delta l_i/2 = 0.03$.

In all the cases in which the plasma elongation is not sufficient ($k < 1.04$) the inclusion of the kinetic data into the equilibrium reconstruction code does not provide significant improvements in the separation of β_p and l_i. This same conclusion applies to the strong transients of the plasma current, as in the early phase of the ramp-up or in the pulses with two levels of plasma current.

In Fig. 14(a) the comparison between β_p^{eq} from the conditioned code ODINP and β_p^{kin} is shown and in Fig. 14(b) the corresponding l_i^{eq} and l_i^{kin} are compared. The database used comes from the general FTU energy confinement database of deuterium plasma at $B_T = 6$ T [31]. The dataset shown in Fig. 14 is further restricted to 342 points, where the 45 discarded points with respect to the database of Fig. 10, which shows the results of the unconditioned code ODIN, have been excluded for the following reasons: 5 shots for minor problems, 30 shots for which the purely toroidal field reference shot is not good enough (although it is acceptable for the unconditioned equilibrium code), giving a systematic offset on the data and finally 10 shots of very low plasma density (with line averaged central electron density $\bar{n}_e \le (4\text{–}5) \times 10^{19}$ m^{-3}) in which the disagreement could be due to the failure of the assumption that $P(\psi) \approx n_e T_e$, owing to a non-negligible effect of the uncoupled ion population upon the shape of the pressure profile.

The least squares fit coefficient in Fig. 14(a) is $\beta_p^{eq} = 0.91\beta_p^{kin}$, with a standard deviation $\Delta\beta_p = 0.03$, which means a spread of $\pm 30\%$ at low β_p, which is reduced to $\pm 7\%$ at high β_p. The least squares fit coefficient in Fig. 14(b) $l_i^{eq}/2 = 0.98 l_i^{kin}/2$, with a standard deviation of $\Delta l_i/2 = 0.03$, which means a spread of 5% at low $l_i/2$ which is reduced to $\pm 3\%$ at high l_i.

The improvement in the agreement of β_p^{eq} and of l_i^{eq} with the kinetic values that is due to the more sophisticated analysis of the ODINP code is very small and is mainly observed on the internal inductance (cf. Figs 10(b) and 14(b)).

The reliability of the estimate of the current density profile J_ϕ obtained by the ODINP code is clarified in Fig. 15, in which the effect of the largest possible variation of the exponents α, β and γ upon the radial behaviour of the reconstructed J_ϕ profile is shown. In the case of the high q_ψ discharges (No. 2728, Fig. 15(a)) the uncertainty is quite small and is concentrated in a narrow central sawtoothing region of the discharge; also in the intermediate and low q_ψ discharges the same conclusion applies, with the difference that the central sawtoothing region became much larger (shot No. 4023, Fig. 15(b), and shot No. 5546, Fig. 15(c)).

It has to be pointed out that the error induced upon the J_ϕ profile by the uncertainties of the magnetic measurements (see Appendix A) and of the density

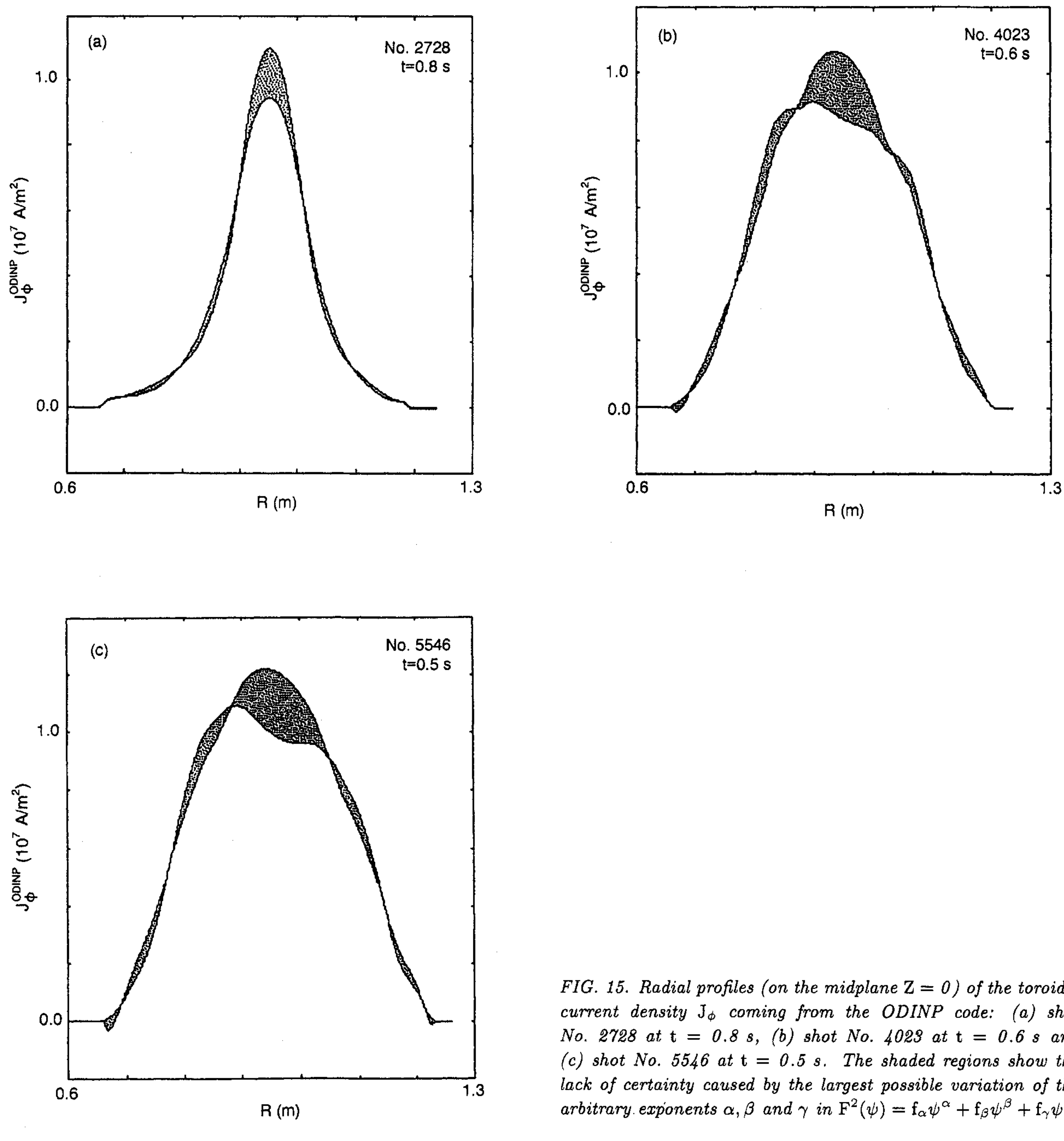

FIG. 15. Radial profiles (on the midplane $Z = 0$) of the toroidal current density J_ϕ coming from the ODINP code: (a) shot No. 2728 at $t = 0.8$ s, (b) shot No. 4023 at $t = 0.6$ s and (c) shot No. 5546 at $t = 0.5$ s. The shaded regions show the lack of certainty caused by the largest possible variation of the arbitrary exponents α, β and γ in $F^2(\psi) = f_\alpha\psi^\alpha + f_\beta\psi^\beta + f_\gamma\psi^\gamma$.

profile (see Appendix B) is much smaller than the effect of the variation of the exponents α, β and γ in Eq. (6).

The effect of the largest possible variation of the exponents α, β and γ upon the radial behaviour of the reconstructed q profile is shown in Fig. 16. Corresponding to the results of Fig. 15, the uncertainty is quite small and is concentrated in a central region roughly within the $q = 1$ surface. It seems that, even if a sizeable indetermination of the value of the safety factor at the plasma axis is still present, the resilience of the q profile to the change of the functional form of the diamagnetic current F is quite significant. On the other hand, Fig. 16 illustrates clearly why the

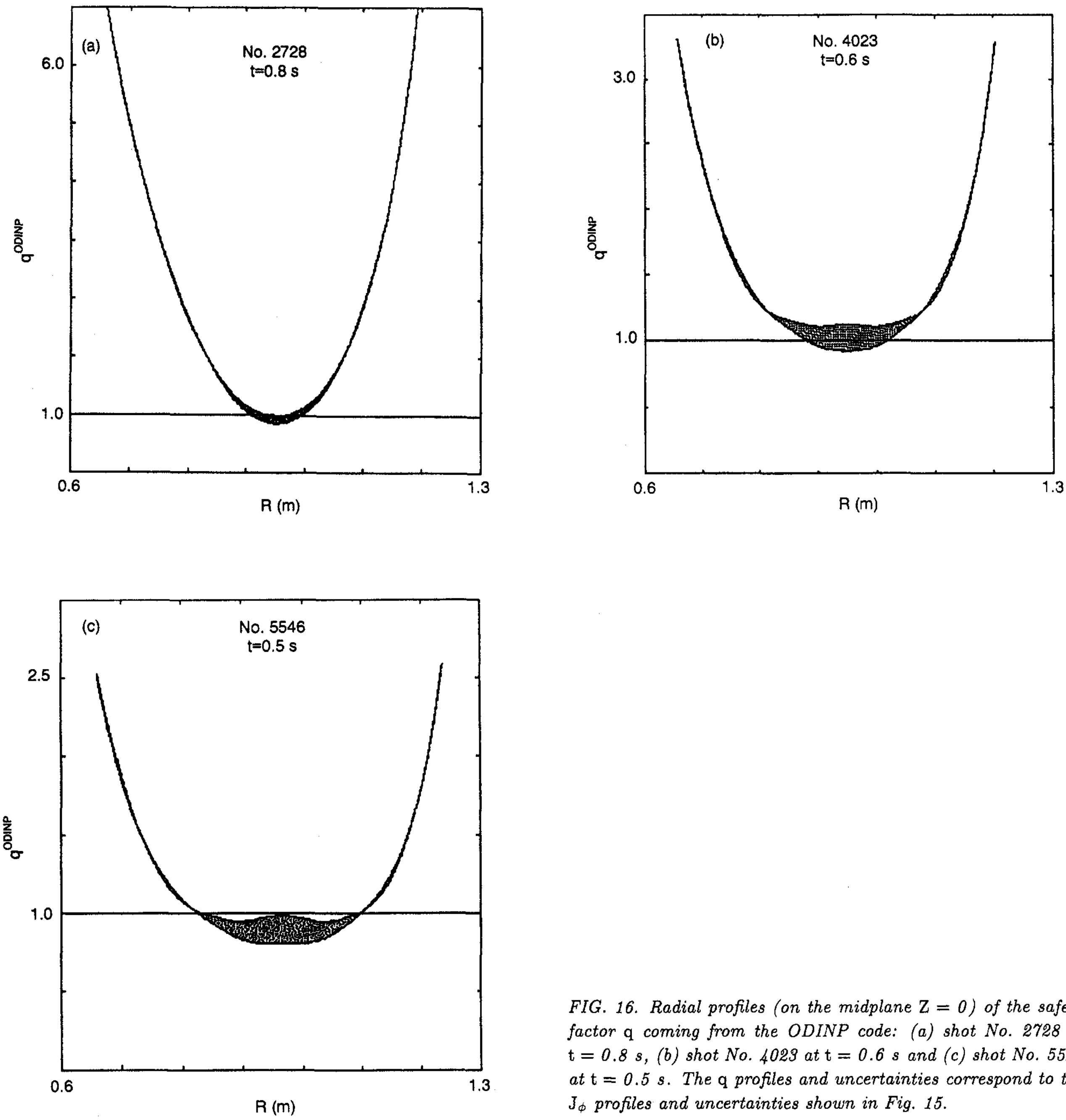

FIG. 16. Radial profiles (on the midplane Z = 0) of the safety factor q *coming from the ODINP code: (a) shot No. 2728 at* t = *0.8 s, (b) shot No. 4023 at* t = *0.6 s and (c) shot No. 5546 at* t = *0.5 s. The* q *profiles and uncertainties correspond to the* J_ϕ *profiles and uncertainties shown in Fig. 15.*

sawtooth activity is not detectable on the equilibrium magnetic measurements: the uncertainties corresponding to the variation of the arbitrary exponents α, β and γ that is performed holding constant the boundary conditions provided by the magnetic measurements produce an uncertainty upon the q value in the central region that is greater than the variation of safety factor that is predicted in the same region by different theoretical models of the sawtooth activity [32–34].

The effect of the measured P profile shape on the reconstructed J_ϕ profiles is shown in Fig. 17 for the same shots as in Fig. 15. In all the sawtoothing discharges the details of the part of the current density

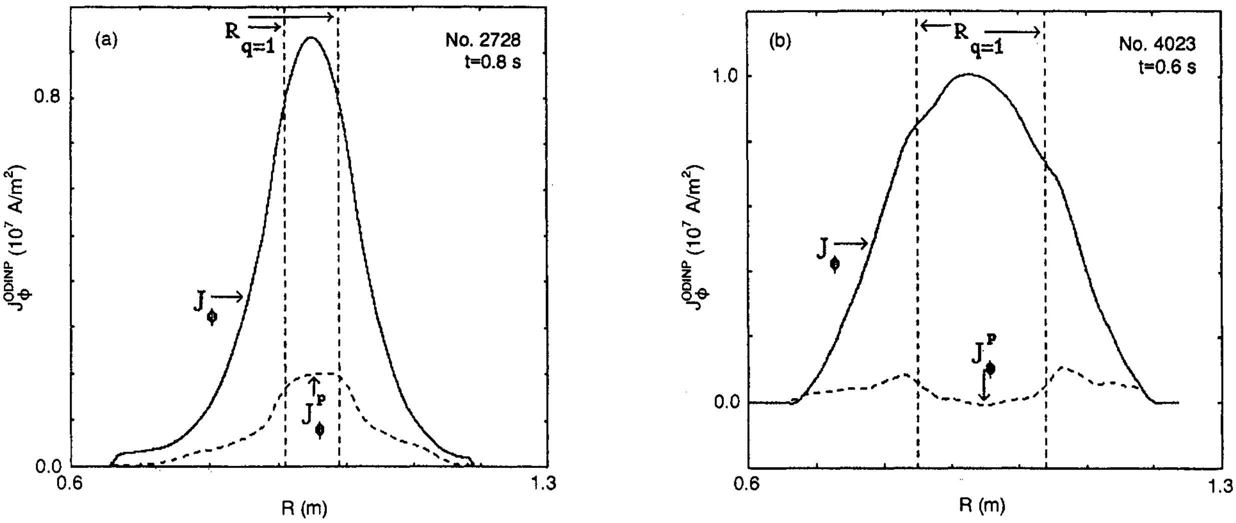

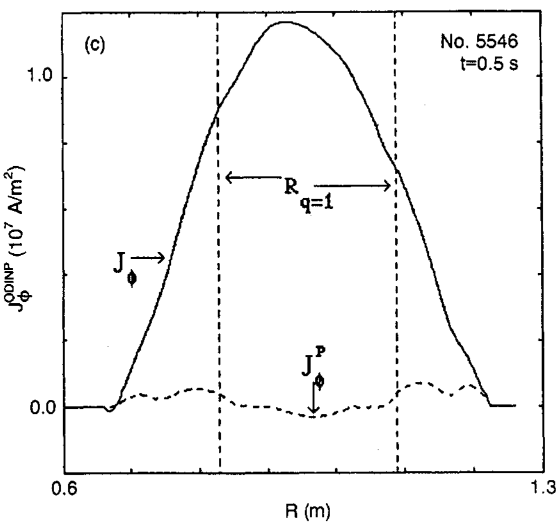

FIG. 17. Radial profiles (on the midplane Z = 0) of the toroidal current density J_ϕ coming from the ODINP code with the standard exponent choice $\alpha = 1.5, \beta = 2.5$ and $\gamma = 3.5$ (solid line). The $J_\phi^P = 2\pi R dP(\psi)/d\psi$ component is also shown (dashed lines) for (a) shot No. 2728 at t = 0.8 s; (b) shot No. 4023 at t = 0.6 s and (c) shot No. 5546 at t = 0.5 s.

profile due to the kinetic pressure $J_\phi^P = 2\pi R \mathrm{d}P(\psi)/\mathrm{d}\psi$ are strongly correlated with the radial position of the $q = 1$ resonant surface. At high q_ψ (Fig. 17(a)) the effect of J_ϕ^P is quite strong and is the determining factor for the correct J_ϕ reconstruction; at low q_ψ (Fig. 17(c)) the effect of J_ϕ^P is quite weak, owing to the low β_p.

In the discharges characterized by a plasma detachment phenomenon (see Fig. 8) the results of the ODINP code improve only very slightly on the results of a purely magnetic analysis: first of all the uncertainties on the n_e profiles (see Appendix B) play their part; then the splitting between β_p and l_i remains uncertain when different choices for α, β and γ are explored; finally the convergence of the ODINP code is often not achieved at the onset of the detachment, confirming that the assumptions that are at the basis of the Grad–Shafranov equation could be violated.

4. VALIDATION OF THE RECONSTRUCTED J_ϕ PROFILES

The reliability of the J_ϕ profile reconstruction obtained from the ODINP code, with the standard exponent choice $\alpha = 1.5$, $\beta = 2.5$ and $\gamma = 3.5$ for the diamagnetic current

$$F^2(\psi) = f_\alpha \psi^\alpha + f_\beta \psi^\beta + f_\gamma \psi^\gamma$$

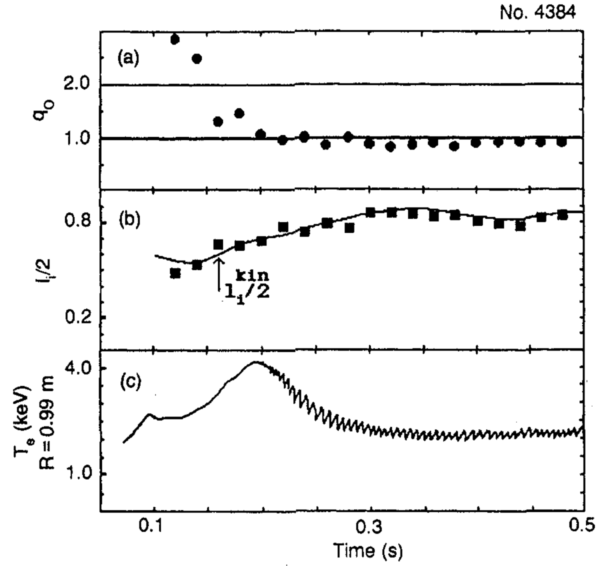

FIG. 18. Shot No. 4384 (I_p = 500 kA, B_T = 6 T, $\bar{n}_e$ = (0.3–0.7) × 10^{20} m^{-3}). Wave forms of (a) safety factor q_0 at the plasma axis (from ODINP), (b) internal inductance $l_i/2$ as computed by ODINP (squares) and by the kinetic data (solid line) and (c) T_e at R = 0.99 m measured by the ECE polychromator. The correspondence between the fall of q_0 below unity and the appearance of the sawtooth relaxations is quite good.

has been checked by a detailed comparison with the observed MHD behaviour of the FTU plasma discharges.

The first MHD phenomenon that has been investigated is the well known sawtooth activity. In Fig. 18 (shot No. 4384, I_p = 500 kA) the time evolution of the safety factor at the plasma axis q_0 is plotted together with the electron temperature near the plasma centre as measured by the ECE polychromator grating [35]. The correspondence between the dropping of q_0 below unity and the appearance of the sawtooth relaxations is quite good (the discrepancy in the timing being of the order of a few tens of milliseconds). Such a good agreement is often lost in the high q_ψ discharges, where the J_ϕ reconstruction is more uncertain (see Fig. 15(a)).

A reasonable agreement is also found between the sawtooth inversion radius (as measured by the ECE polychromator) and the width of the q = 1 surface computed by the ODINP code, at least in the low q_ψ plasma pulses (see Fig. 19 for shot No. 5546). This is further confirmed as twin discharges can be easily produced (at least down to q_ψ = 4); they differ only in the presence (as in shot No. 4965) or absence (as in shot No. 4964) of the sawtooth oscillations, but have the same I_p, $\bar{n}_e$ and B_T. The different behaviour in the central region corresponds to a q_0 value of the order of 1.5 for the sawtooth-free pulse as opposed to a q_0 value of the order of 1.0 for the sawtoothing one (see Fig. 20). As can be seen in Fig. 21, the current distribution is almost the same in the external part of the plasma column.

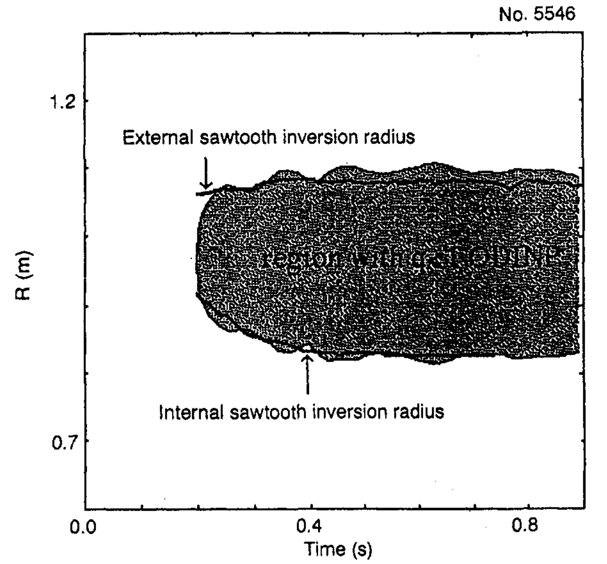

FIG. 19. Shot No. 5546 (q_ψ = 2.5). Wave forms of the internal and external sawtooth inversion radii (from the ECE polychromator) compared with the region (shaded) in which ODINP finds q < 1.

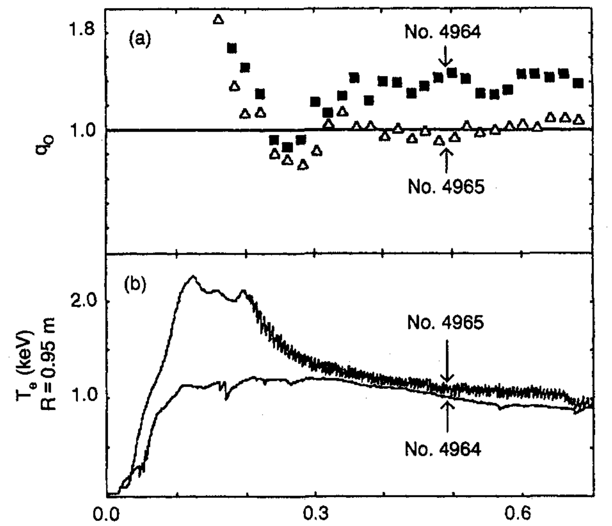

FIG. 20. Shots Nos 4964 without sawteeth and 4965 with sawteeth (both with I_p = 700 kA, B_T = 6 T, $\bar{n}_e$ = (0.5–1.7) × 10^{20} m^{-3}). Wave forms of (a) safety factor q_0 at the plasma axis (from ODINP) and (b) T_e at R = 0.95 m measured by the ECE polychromator.

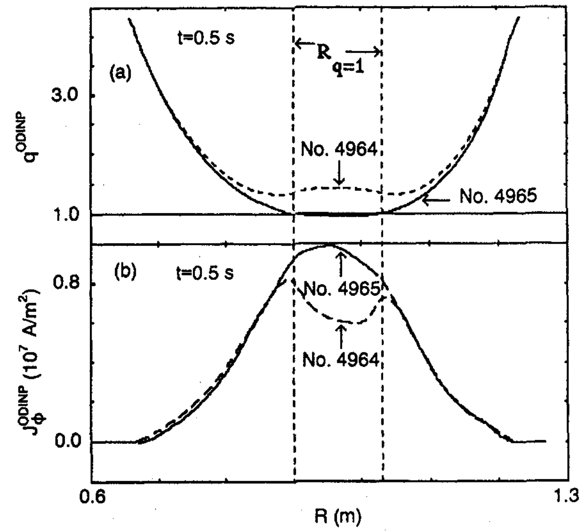

FIG. 21. (a) Shots Nos 4964 without sawteeth and 4965 with sawteeth at t = *0.5s. Radial profiles (on the midplane* Z = *0) of (a) safety factor* q *and (b) toroidal current density* J_ϕ *as computed by ODINP. The extension of the* q = *1 region for shot No. 4965 is also reported.*

In ohmic discharges the current density profile determined by the ODINP code, in the presence of the sawtooth activity, has been compared with the predictions of the Spitzer resistivity theory [36], based on the T_e and n_e profiles, assuming a constant Z_{eff} radial profile ($J_\phi^{SP} \approx T_e^{3/2}$, apart from negligible Coulomb logarithm corrections). The result was an impressive agreement between J_ϕ and $T_e^{3/2}$ for all the q_ψ values (see Fig. 22), with large uncertainties only in the central region of the discharge, in which the sawtooth activity affects the current density profile.

It has to be remarked that the $T_e^{3/2}$ information is not an input at all into the ODINP code, where only the product $n_e T_e$ is used in one of the two sources (Eq. (6)) of the Grad–Shafranov equation: so the good agreement between J_ϕ and $T_e^{3/2}$ does not imply any risk of tautology.

A comparison with the neoclassical theory of plasma resistivity [37] is under way [38] and the typical result is that the neoclassical current density profile is 40–60% higher than the current density profile obtained from ODINP. However, this comparison is complicated by the possibility that the usual short period (5 to 7 ms) sawtooth activity of FTU [31], by producing a hollow profile of toroidal electric field [39], could make the neoclassical current density profile similar to the Spitzer one. On the other hand, it is worthwhile to reiterate that the results of the kinetic–magnetic

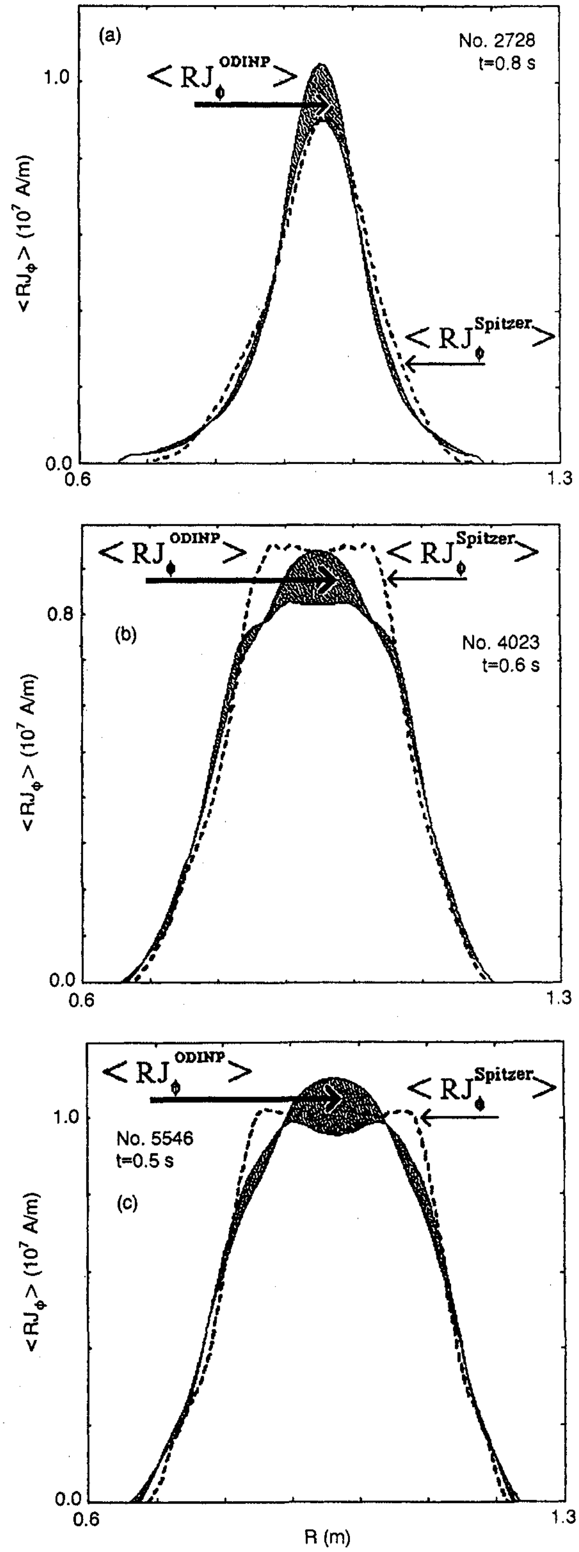

FIG. 22. (a) Shot No. 2728 at t = *0.8s, (b) shot No. 4023 at* t = *0.6s and (c) shot No. 5546 at* t = *0.5s. Comparison between the flux averaged* $\langle RJ_\phi \rangle$ *profiles as computed by assuming the Spitzer resistivity (dotted lines) and by the ODINP code (shaded regions accounting for the largest possible variation of the exponents* α, β *and* γ *in* $F^2(\psi) = f_\alpha \psi^\alpha + f_\beta \psi^\beta + f_\gamma \psi^\gamma$*).*

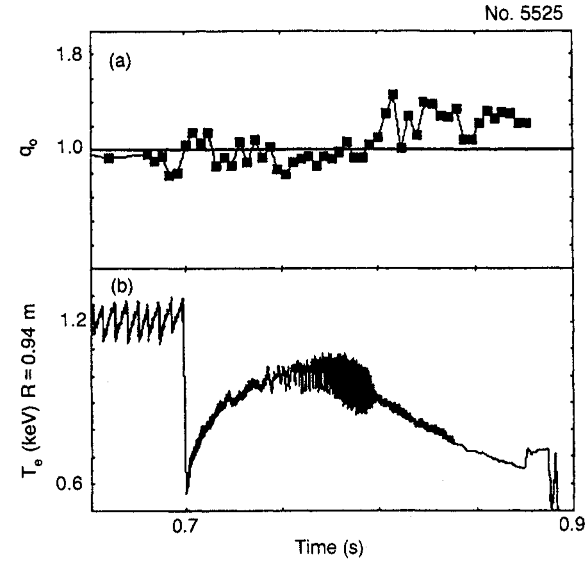

FIG. 23. Shot No. 5525 (I_p = 900 kA, B_T = 6 T, $\bar{n}_e$ = (1.5–2.3) × 10^{20} m^{-3}). Wave forms of (a) safety factor q_0 at the plasma axis (from ODINP) and (b) T_e at R = 0.94 m measured by the ECE polychromator, showing the snake oscillation that is induced by a deuterium pellet injection at t = 0.7s.

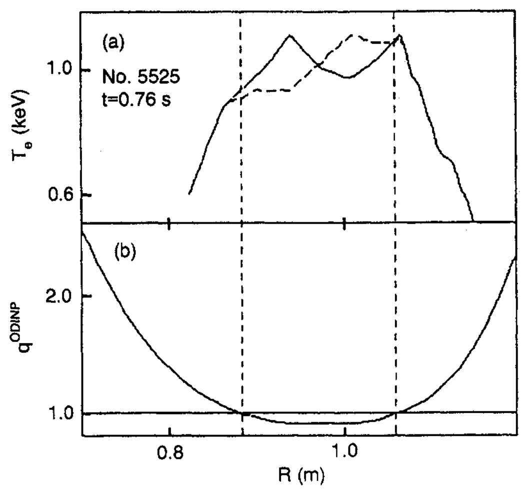

FIG. 24. Shot No. 5525 at t = 0.76s. Profiles of T_e at opposite phases of the snake oscillation (as measured by the ECE polychromator) and q (from ODINP) during the snake.

reconstruction code have an uncertainty in the value of J_ϕ in the central region of the sawtoothing discharges (see Fig. 15) that is of the same magnitude, or larger, than the effect that reconnection theories [32–34] predict for the current density variation during the sawtooth relaxations.

Another MHD phenomenon that has been investigated is the snake oscillation [40] that is often observed in pellet injected FTU discharges when q_ψ is lower than 4 [38]. The time behaviour of q_0 during the snake phase of pellet injected shot No. 5525 (I_p = 900 kA) shows a good correspondence with the evolution of the phenomenon (see Fig. 23). In this case (Fig. 24), the structure of the snake perturbation on the T_e profile is found to be strictly correlated to the width of the $q = 1$ region.

A further validation is obtained by trying to reproduce the qualitative behaviour of the MHD Mirnov oscillations [41–43], as they are detected by the poloidal field coils (see Appendix A) located outside the vacuum vessel of FTU. To achieve this aim, the J_ϕ profile coming from the ODINP code has been projected on a cylindrical geometry to be used as the input data of a cylindrical tearing stability code [43], able to provide an evaluation of the linear tearing mode Δ' quantity [44], for given poloidal (m) and toroidal (n) mode numbers. Figure 25 shows the time evolution of Δ' for an FTU discharge with pellet injection (shot No. 4959, I_p = 700 kA). The bursts of MHD activity observed in the post-pellet phase are associated with a destabilization of the ($m = 2, n = 1$) and ($m = 3, n = 2$) tearing modes, as predicted by the cylindrized J_ϕ profile.

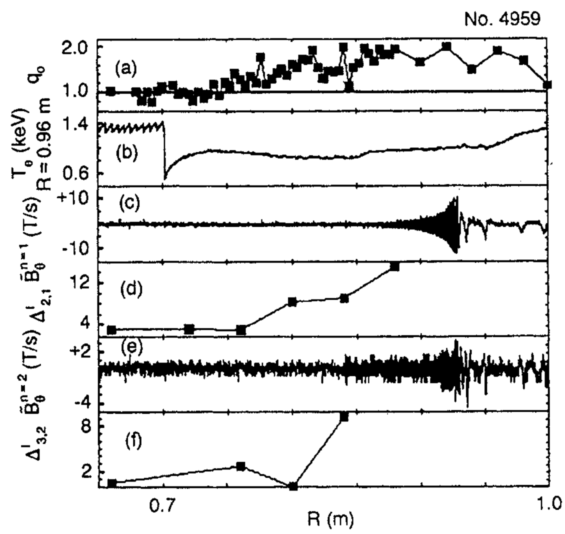

FIG. 25. Shot No. 4959 (I_p = 700 kA, B_T = 6 T, $\bar{n}_e$ = (1.2–2.3) × 10^{20} m^{-3}) with deuterium pellet injection at t = 0.7 s. Wave forms of (a) safety factor q_0 at the plasma axis (from ODINP), (b) T_e at R = 0.96 m measured by the ECE polychromator, (c) fluctuating field $\tilde{B}_\theta$ with toroidal number n = 1, (d) tearing mode linear $\Delta'_{2,1}$, as calculated from the cylindrized ODINP J_ϕ profile, (e) fluctuating field $\tilde{B}_\theta$ with toroidal number n = 2 and (f) tearing mode $\Delta'_{3,2}$, as calculated from the cylindrized ODINP J_ϕ profile.

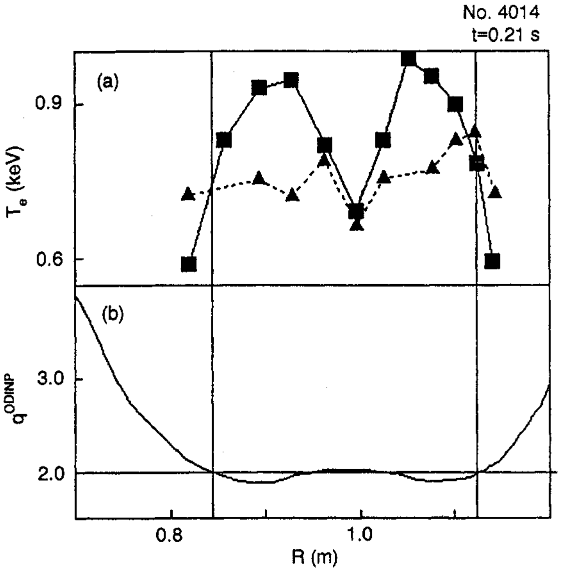

FIG. 26. Shot No. 4014 (I_p = 700 kA, B_T = 6 T, $\bar{n}_e = 0.7 \times 10^{20}$ m^{-3}) at t = 0.21 s: (a) T_e profile (as measured by the ECE polychromator) just before (squares) and just after (triangles) the sawtooth crash and (b) safety factor q profile (from ODINP) showing the q = 2 double resonance.

Finally the magnetic reconnections between double resonant surfaces have provided an interesting validation of the J_ϕ profile reconstruction. Bursts of double resonant reconnection are often observed in FTU [45], either when the plasma internal inductance is still rising after the current has reached its plateau value or after a pellet injection. These relaxations are associated with hollow temperatures profiles and the temperature variation resembles that of the usual sawtooth activity, in the sense that it exhibits a sudden crash, a well defined inversion radius and a diffusive behaviour outside the mixing radius, with the remarkable exception that it vanishes near the plasma magnetic axis. Figure 26 shows the T_e profiles, as observed by the ECE grating polychromator, just before and just after a crash, together with the reconstructed q profile (shot No. 4014, I_p = 700 kA). The correspondence between the external $q = 2$ surface and the sawtooth inversion radius is quite good.

5. CONCLUSIONS

The experimental equilibrium reconstruction of the FTU tokamak plasmas has been obtained by using the magnetic measurements alone as well as by including the shape of the electron pressure profile.

In the absence of transient currents in the vacuum vessel and of plasma detachment and if q_ψ is not too high and the density and $\beta_p + l_i/2$ not too low, the magnetic data alone have appeared to be able to allow for a good evaluation of integral plasma quantities such as the poloidal beta and the internal inductance, if the elongation of the plasma cross-section is high enough to remove the cylindrical degeneracy.

When the information about the shape of the electron pressure profile is added to the magnetic data, a reasonable estimate of the current density profile can be obtained, even without the need of any direct measurement of the poloidal magnetic field profile.

The reliability of the J_ϕ profile reconstructed by the kinetic–magnetic version of the code has been explored and validated by analysing the correspondence with the MHD behaviour of the plasma pulses, at least for q_ψ values less than 4. In these conditions it appears that, even if a relevant error bar on the q_0 value is still present ($\Delta q_0 \approx \pm 0.2$), the position of the internal rational q resonances can be evaluated with a remarkable degree of accuracy.

Further improvements of the ODINP code should be possible in the near future. The electron temperature profiles coming from the Thomson scattering diagnostics [46] will be added to the code inputs to attempt the J_ϕ reconstruction in plasma pulses with lower hybrid additional heating [47]. The information about the location of the $q = 1$ surfaces (assumed to be equal to the sawtooth inversion radius) can easily be added to the code, aiming at an increase in the q profile determination accuracy for the sawtoothing discharges. Finally, an integrated measurement of the poloidal field profile will be operative on FTU in the near future by using a five channel Faraday effect polarimeter. These diagnostics, when integrated with the magnetic data and possibly also with the electron plasma pressure profile, should allow a more refined determination of the safety factor profile.

Appendix A

THE MAGNETIC DIAGNOSTICS OF THE FTU TOKAMAK

The magnetic measurements of FTU are based on the standard technique of axisymmetric equilibrium magnetic measurements [48, 49], in which full voltage loops and saddle coils measure the poloidal flux function $\psi = 2\pi R A_\phi$ and poloidal pick-up coils measure the normal derivative $\partial\psi/\partial n$ over a contour enclosing the plasma cross-section.

These two items of data are the Cauchy conditions for the ill posed magnetostatic problem of finding the

(a)

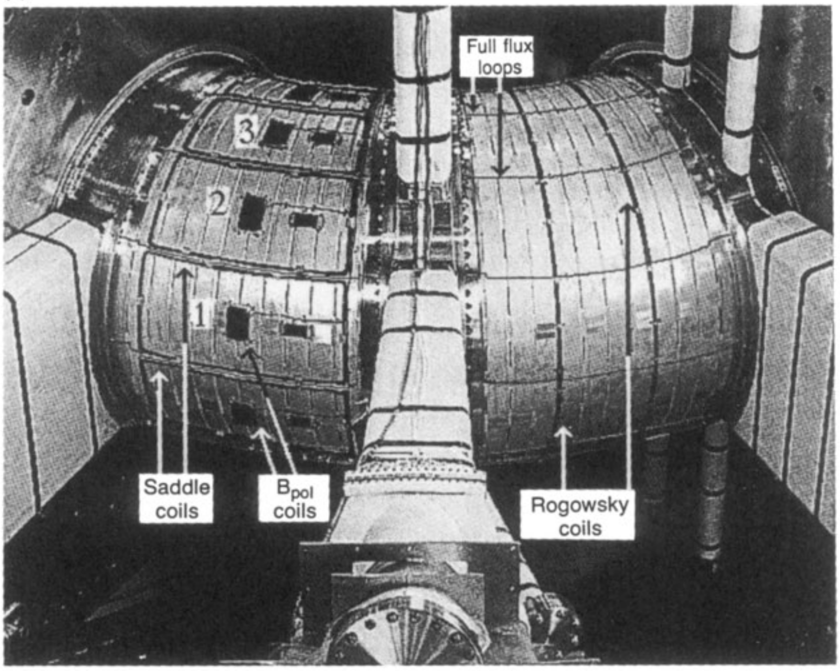

(b)

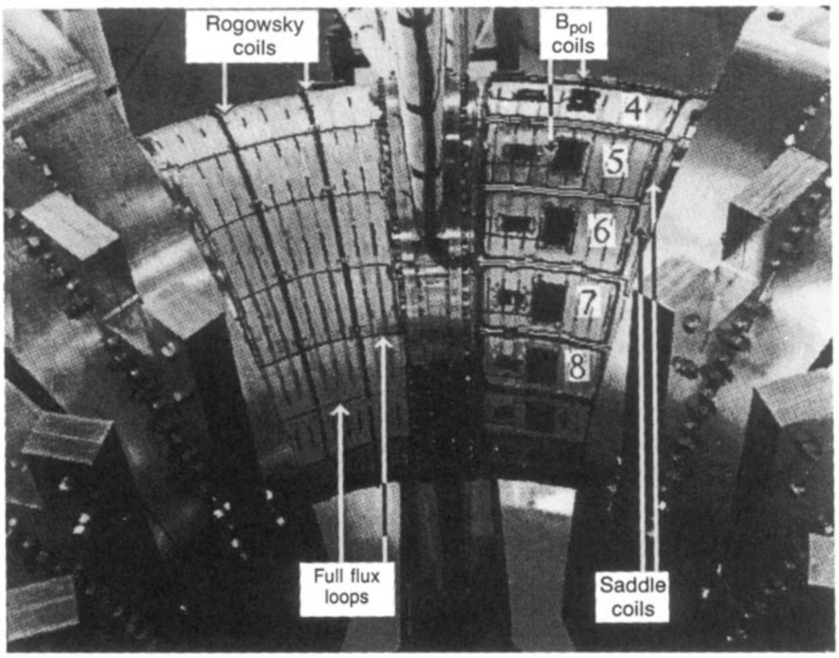

FIG. 27. Sectors Nos 10 and 11 of the FTU vacuum vessel and the interposed port No. 11 before introduction into the corresponding magnet modules, photographed during the machine assembly: (a) view from outboard of the torus and (b) view from inboard of the torus. Sector No. 10 is covered by 16 saddle loops; at the centre of each saddle a poloidal field coil is fixed. The numbers refer to the ordering of the saddle and poloidal field coils. Sector No. 11 houses two Rogowsky coils. The full flux loops can be seen to run along parallels of the torus in the empty space between adjacent saddles. Comparing the inboard and the outboard regions of the torus, it is quite clear that the poloidal extension of the saddle coils and the distribution of the poloidal field coils is not uniform in arc length; instead both are equally spaced in the poloidal angle of the fully toroidal co-ordinates.

plasma boundary [50], starting from the measurement contour. The plasma boundary is derived by following the truncated multipolar expansion (Eq. (3)) that fits the measurements and by assuming that the last plasma magnetic surface is the first closed magnetic surface that intersects any material object.

All the magnetic probes are located outside the circular cross-section vacuum vessel, on a toroidal contour with major radius $R_{\mathrm{pr}} = 0.935$ m and minor radius $a_{\mathrm{pr}} = 0.356$ m. The L/R high frequency cut-off of the vessel for the equilibrium fields and fluxes is of the order of 1 kHz. The standard magnetic measurements are composed of 16 full voltage loops and of four replicas of 16 poloidal pickup coils and 16 saddle coils at 4 toroidal positions around the vacuum vessel (see Fig. 27).

Usually the measurements of the 16 saddles and of the 16 pick-up coils lying at a fixed toroidal position are used. An average of these measurements and the corresponding ones obtained from the toroidally opposite sector is performed only in the discharges affected by quasi-stationary modes [30], in order to analyse the axisymmetric part of the equilibrium.

The poloidal pick-up coils are all equal and are equally spaced in the poloidal angle of the fully toroidal co-ordinates [21], so their distribution is not uniform in the arc length of the measurement contour (see Fig. 27). The calibrated product of the area times the number of turns of each poloidal pick-up coil is within $\pm 1\%$ of the design value. The main systematic error that affects their measurements is the spurious pick-up of toroidal field caused by misalignments: to remove it, one has to subtract the signal of a purely toroidal field reference shot. The agreement between the plasma current, as measured by three Rogowsky coils, and the plasma current, as derived from the line integral of the poloidal field measured by the pick-up coils, is within $\pm 1\%$, at least when a negligible current flows in the vacuum vessel.

The poloidal extension of the saddle coils is similarly not uniform in the arc length of the measurement contour; as a matter of fact all the saddles are poloidally evenly spaced in the fully toroidal co-ordinates (see Fig. 27). The toroidal contours of the saddles follow rigorously a section of the torus at $\phi =$ constant, but the poloidal contours provide an empty space in between all the adjacent saddles to allow for the passage of the 16 voltage loops that run around the machine. These empty spaces introduce geometrical correction factors between 1.04 and 1.09 upon the $\Delta\psi$ measured by each saddle. The main systematic error that affects the measurements of the saddle coils is the spurious pick-up of toroidal field that results from the interplay between the misalignments of the saddles and the time evolution of the $n = 12$ and $n = 24$ components of the ripple field produced by the toroidal field magnet. The time evolution of the toroidal field ripple is mainly due to skin currents in the magnet itself. To remove the spurious pick-up, one has to subtract the signal of a purely toroidal field reference shot. A less important systematic error is a very small nonzero sum of the 16 saddle signals, that remains after the toroidal pick-up has been cured; this negligible error of closure is in any event redistributed evenly on all the 16 saddles.

The 16 loop voltages do not exhibit spurious pick-up of toroidal field. However, because of the obstructions offered by the various ports, not all of the loop voltages can run smoothly along parallel circles around the torus. So they are affected by unknown errors due to the detours they have to make around the ports, although a systematic compensation has been attempted by alternating the direction of the detour between adjacent ports. As a consequence, only the signal of one voltage loop that runs perfectly along a parallel circle of the torus and lies immediately below the inner equatorial plane has been used as the reference point for the ψ measurement. The variation of ψ around the poloidal angle is obtained by the sequential addition of the $\Delta\psi$ measured by the 16 saddle coils.

The method by which the toroidal multipolar expansion of the magnetic configuration is derived is exactly the one detailed in Ref. [1], i.e. a Fourier analysis that determines separately, order by order, the multipolar moments. A fixed toroidal co-ordinates centre

$$\sqrt{(R_{\mathrm{pr}}^2 - a_{\mathrm{pr}}^2)} = R_0 = 0.864 \text{ m}$$

has been used.

In the open vacuum magnetic configurations, which are obtained without a plasma by feeding currents into the various poloidal windings of FTU, both the flux measurements alone as well as the field measurements alone provide two independent boundary conditions to the well posed Dirichlet or Neumann magnetostatic problems for the domain inside the measurement contour. In both these cases, one can solve the two problems independently by using the appropriate measured boundary condition and then one can calculate the other boundary condition; the result is that the correspondence between fields and fluxes is within $\pm(1\text{–}2)\%$.

In the presence of the plasma, the multipolar expansion that starts from the multipolar order $m = 0$, must be truncated at a certain order $m = m_{\max}$. As was detailed in Fig. E1 of Appendix E in Ref. [1], the determination of the $m = 3$ internal multipolar moment should be accurate within ±12.5% over the whole range of $\beta_p + l_i/2$, assuming an uncertainty of ±1% on the measured values of ψ and B_{pol}. On the other hand, with the same assumptions, the accuracy on the $m = 4$ moment is less than ±50%, when $\beta_p + l_i/2$ is greater than 0.5, and less than ±25% only when $\beta_p + l_i/2$ is greater than 0.8. Remembering that all these resulting uncertainties scale up linearly with the uncertainty on the measurements of ψ and B_{pol} (see Fig. E3 of Ref. [1]), the correct determination of the $m = 4$ multipolar moment remains quite dubious in FTU.

On the other hand, the $m = 4$ multipolar moments are not used in the equilibrium reconstruction codes and, as a Fourier method is used, the uncertainties on the high order multipolar moments do not influence the determination of the lower order ones. Therefore only the uncertainties in the low order multipolar moments ($m = 0$ to $m = 3$) propagate into uncertainties in the parameters inferred from the equilibrium reconstruction codes. The effects of such errors have been discussed in Ref. [1], with the assumption of arbitrary relative errors on the measured values of ψ and B_{pol}. As a consequence it is the level of the actual experimental errors on ψ and B_{pol} that has to be assessed; the best way to infer this is to compare the measured data with the best fit obtained by truncating the multipolar expansion at the order $m_{max} = 3$ or $m_{max} = 4$.

The quality of the fit for the flux measurements in shot No. 4023, obtained by the toroidal multipolar expansion in the presence of the plasma, is shown in Fig. 28. The correspondence between the flux measurement as inferred from the saddles and as directly measured from the voltage loops is quite good. The effect of moving the truncation of the multipolar expansion from the order $m_{max} = 3$ to $m_{max} = 4$ produces an uncertainty of ±3% upon the fit of $\psi_{max} - \psi_{min}$.

The quality of the corresponding fit for the poloidal field measurements is shown in Fig. 29. The effect of moving the truncation of the multipolar expansion from the order $m_{max} = 3$ to $m_{max} = 4$ produces an uncertainty of ±3% upon the fit of B_{pol}.

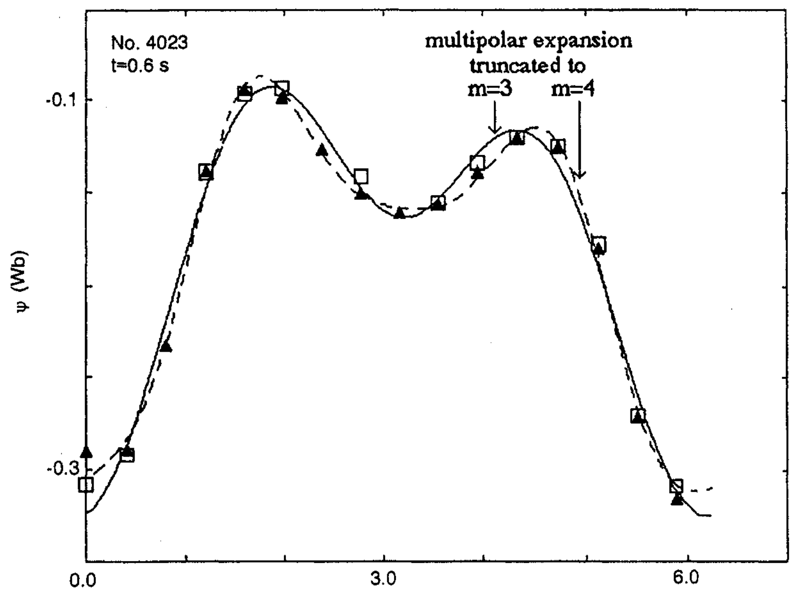

FIG. 28. Shot No. 4023 at $t = 0.6$ s ($I_p = 850$ kA, $B_T = 6$ T, $q_\psi = 3.3$). Behaviour of the flux function ψ measured by the saddle coils (triangles) and by the full voltage loops (squares), along with the toroidal multipolar expansion fit to ψ, truncated to the order $m = 3$ (solid line) and $m = 4$ (dashed line), as a function of the poloidal angle $\tilde{\omega}$ of the fully toroidal co-ordinates. $\tilde{\omega} = 0$ corresponds to the outboard equator of the toroidal vacuum vessel and $\tilde{\omega} = \pi$ to the inboard one. The loop voltages Nos 3, 7 and 9 do not show up as the loops have unfortunately been open since the assembly of the machine, whereas the loop voltage No. 10 is used as the reference point for the ψ measurement.

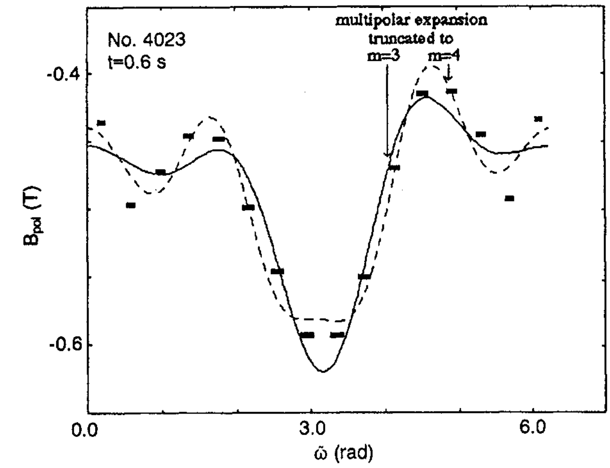

FIG. 29. Shot No. 4023 at t = *0.6 s. Behaviour of the poloidal field* B_{pol} *measured by the poloidal field coils, along with the toroidal multipolar expansion fit to* B_{pol}*, truncated to the order* m = *3 (solid line) and* m = *4 (dashed line), as a function of the poloidal angle* $\tilde{\omega}$ *of the fully toroidal co-ordinates. The rectangles show that the* $\tilde{\omega}$ *extension of the poloidal field coils is not uniform, whereas the poloidal arc length extension is the same.*

However, from the point of view of the equilibrium reconstruction, the relevant uncertainty is not the one of the fit at the position of the measurement contour but the resulting uncertainty at the position of the plasma boundary. The uncertainty in the position itself of the plasma boundary turns out to be at most ±2.5 mm (see Fig. 30), and so ±1% of the minor radius of the discharge. The uncertainty in the value of $B_{\rm pol}$ on the plasma boundary is also ±1% (see Fig. 31).

It should be remarked that both the unconditioned (ODIN) and the conditioned (ODINP) equilibrium reconstruction codes are systematically executed on each shot of FTU. The equilibria are solved with a time step of 20 ms, thus producing an average of 70 equilibrium time slices for every shot, which are fed into the electronic archive of the elaborated data. All these data are easily retrievable through standard FORTRAN routine calls by any experimentalist who needs to use the equilibrium reconstruction. The average time that is necessary on an IBM 3090/9000T mainframe for producing all the equilibrium elaborated data for one plasma shot is on average five minutes of CPU time: which means an effective time shorter than the average interval between shots (15 min), if the IBM mainframe is not overloaded. The reliability of the equilibrium reconstruction code is such that it has presently become the main diagnostic for any malfunctioning of the equilibrium magnetic measurements: in all those cases in which the code did not converge for a few successive shots the cause was invariably an unnoticed failure of some electronic hardware module which was promptly identified and replaced.

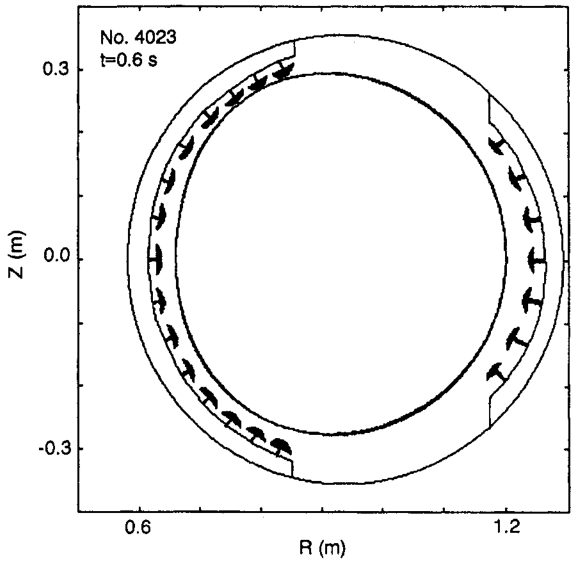

FIG. 30. Shot No. 4023 at t = *0.6 s. Plasma last closed magnetic surface as reconstructed from the equilibrium magnetic measurements, with the toroidal multipolar expansion truncated to both the orders* m = *3 and* m = *4: the variable thickness of the boundary indicates the corresponding uncertainty in the plasma position. The 'mushroom' symbols outline the shape of the inner and outer poloidal limiters that sit on port No. 1 of FTU, and the outermost circle represents the vacuum vessel.*

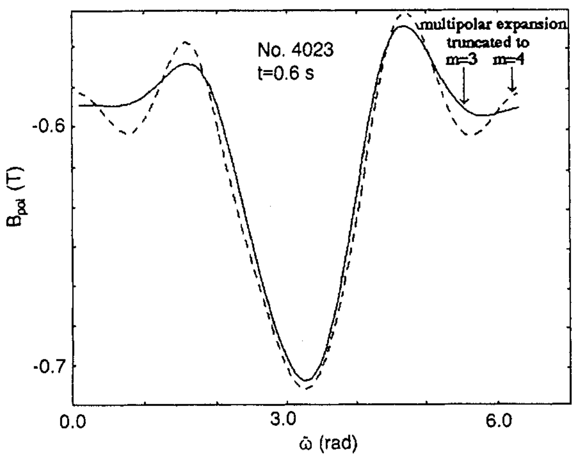

FIG. 31. Shot No. 4023 at t = *0.6 s. Behaviour of the poloidal field* B_{pol} *on the plasma boundary shown in Fig. 30, as a function of the poloidal angle* $\tilde{\omega}$ *of the fully toroidal co-ordinates. The truncation of the multipolar expansion at order* m = *3 gives the poloidal field* B_{pol} *drawn as a solid line and the truncation to* m = *4 is shown as a dashed line.*

Appendix B

INVERSION OF THE n_e PROFILE BY USING THE ZERNICKE POLYNOMIAL TECHNIQUE

The equilibrium reconstruction code ODIN, using the equilibrium magnetic measurements alone, is able to produce a correct identification of the magnetic topology that labels the plasma by a flux function ψ^{ODIN} (Fig. 32, full lines, shot No. 2728); however, it cannot provide the exact value of the flux function ψ, which is better approximated by the flux function ψ^{ODINP} produced by the conditioned code ODINP (Fig. 32, dashed lines). Nevertheless, the real flux function ψ is, within a reasonable approximation, a function of ψ^{ODIN}; this is even true for a high q_ψ shot like No. 2728 (Fig. 33) where, as discussed in Section 2, the discrepancy between ODIN and ODINP is among the largest so far obtained. Correspondingly, as, in an MHD equilibrium without plasma flows, the pressure is a function of the flux function $P(\psi)$ and moreover as, in the collisionless high temperature regime, the very high parallel thermal conductivity makes the temperature a function of ψ, the electron density must also be a function of ψ, $n_e = n_e(\psi)$. Consequently, one can assume that $n_e = n_e(\psi^{\mathrm{ODIN}})$ for all practical purposes concerning the inversion of the interferometric line integrated signals: in the remainder of this Appendix, as well as in the main body of the paper, no other distinction will be maintained between ψ and ψ^{ODIN} in the matter of the n_e profile.

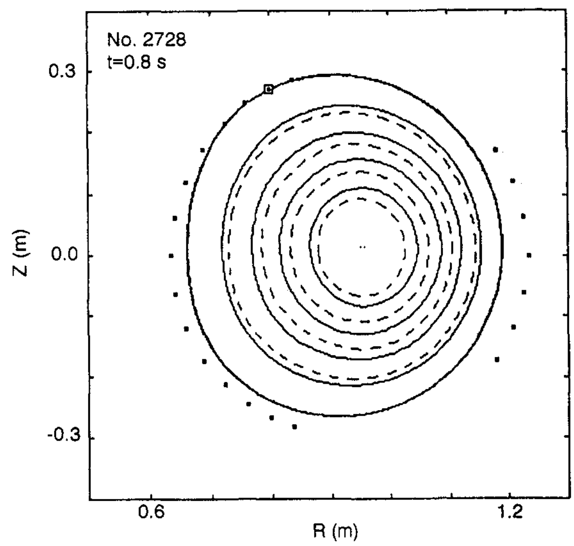

FIG. 32. Shot No. 2728 at t = 0.8 s. Contour map of the poloidal flux function ψ^{ODIN}, as identified from the unconditioned code ODIN: the solid curves correspond to $\psi^{ODIN} = \mathrm{k}\psi^{ODIN}_{axis}/5$, with k = 0 to 5. Contour map of the poloidal flux function ψ^{ODINP}, as identified from the kinetic–magnetic code ODINP: the dashed curves correspond to $\psi^{ODINP} = \mathrm{k}\psi^{ODIN}_{axis}/5$ and k = 0 to 5. The tips of the 'mushrooms' of the poloidal limiters are shown as points and the limiter–plasma contact point is identified by a small square.

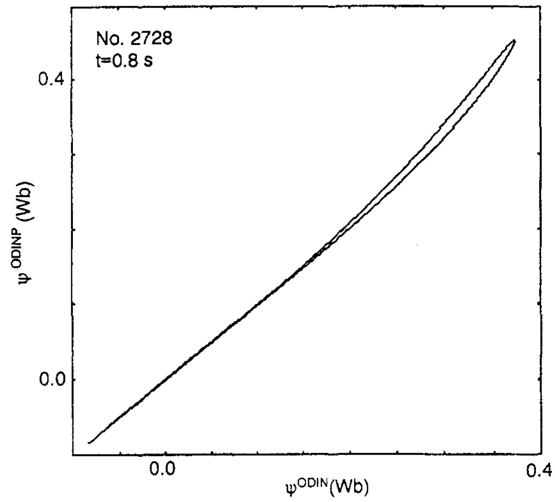

FIG. 33. Shot No. 2728 at t = 0.8 s. Relationship between ψ^{ODINP} and ψ^{ODIN} of Fig. 32, as observed on the midplane Z = 0.

The determination of the functional form of $n_e(\psi)$ from a limited number of interferometric signals is performed by a truncation of the power expansion,

$$n_e(\psi) = n_0 + \sum_{k=1}^{K} n_k \psi^{k/2} \tag{7}$$

The choice of expanding $n_e(\psi)$ in terms of $\psi^{1/2}$, and not in terms of ψ, comes from the result that, in the large majority of cases in which the electron density profile is not peaked, the density profile behaves essentially like $\psi^{1/2}$, and so a description in terms of integer powers of ψ would require too many terms.

The channels of the DCN interferometer [25] measure the line integrated densities

$$D_j = \int_{l_j} n_e \, \mathrm{d}l_j$$

along the vertical chords at $R = R_j$ with length l_j through the FTU plasma; as there are just five of these, a very limited number K of coefficients n_k in formula (7) can be determined.

The technique of inversion is based on the Zernicke polynomials [26–28], of angular order m and radial order l, that are defined on the polar co-ordinates (ρ, η) of the unitary circle as

$$Z_m^l(\rho) = \sum_{s=0}^{l} (-1)^s \begin{pmatrix} m+2l-s \\ m+l-s \end{pmatrix} \begin{pmatrix} l \\ s \end{pmatrix} \rho^{m+2l-2s} \quad (8)$$

These polynomials constitute a good basis for comparing local quantities $g(\rho, \eta)$ over the unit circle with their line integrated values $f(p, \phi)$ along a chord with impact parameter p and impact angle ϕ. The correspondence between components of the angular (respectively, η and ϕ) Fourier expansions $g_m^{c/s}(\rho)$ and $f_m^{c/s}(p)$ is

$$g_m^{c/s}(\rho) = \sum_{l=0}^{\infty} (m+2l+1) a_m^{l,c/s} Z_m^l(\rho) \quad (9a)$$

$$f_m^{c/s}(p) = 2 \sum_{l=0}^{\infty} a_m^{l,c/s} \sin[(m+2l+1)\cos^{-1}(p)] \quad (9b)$$

The reconstructed equilibrium is enclosed within a Zernicke circle, centred on the plasma magnetic axis $(R_{\rm axis}, Z_{\rm axis})$, with a radius $R_{\rm d}$ that includes the plasma boundary. The half-integer powers of the flux function $\psi^{k/2}$ are expanded in Zernicke polynomials with respect to this circle,

$$\psi^{k/2}(\rho, \eta) = \sum_{m=0}^{M} \sum_{l=0}^{L} (m+2l+1) \times (a_m^{l,c}(k)\cos(m\eta) + a_m^{l,s}(k)\sin(m\eta)) Z_m^l(\rho) \quad (10)$$

The truncation of the expansion is set to $M = 6$, $L = 11$, which guarantees an accuracy of 1% on ψ. Fictitious measurement chords inside the Zernicke circle, with zero line integrated densities, have to be added outside the plasma as a regularization of the oscillatory behaviour of the high order Zernicke polynomials. Using Eq. (7), where the density at the boundary n_0 is set to 10% of the central chord of the DCN interferometer, and adding eight zero-measurement chords outside the plasma, the following overdetermined system is solved for $j = 1, 13$ (5 DCN chords + 8 zero chords):

$$(D_j - n_0 l_j)/R_d = 2\sum_{k=1}^{K} n_k \left[\sum_{m=0}^{M} \sum_{l=0}^{L} [a_m^{l,c}(k)\cos(m\phi_j) + a_m^{l,s}(k)\sin(m\phi_j)] \sin[(m+2l+1)\cos^{-1}(p_j)] \right] \quad (11)$$

where p_j and ϕ_j are the impact parameters and the

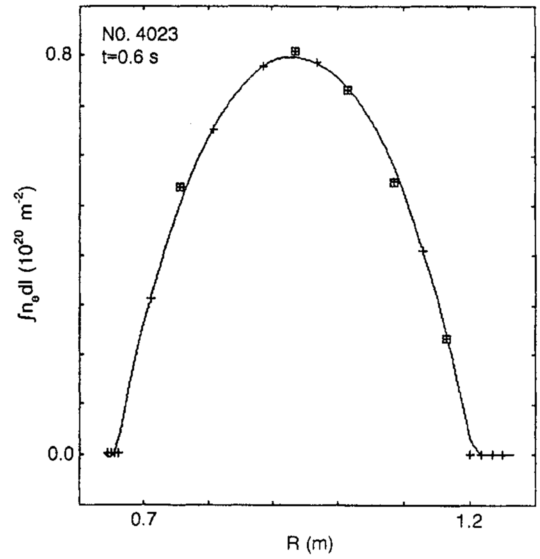

FIG. 34. Shot No. 4023 at t = 0.6 s. Line integrated densities $D_j = \int_{l_j} n_e \, dl_j$, along the vertical chords at $R = R_j$ with length l_j through the FTU plasma, as measured from the DCN interferometer chords (squares), as calculated on the flux function mirrored chords after the preliminary inversion (crosses), along with zero chords outside the plasma (crosses). They are compared with the line integral of the final density inversion $n_e(\psi) = n_0 + n_1\psi^{1/2} + n_2\psi + n_3\psi^{3/2}$, shown as a solid line as a function of the major radius on the symmetry plane $Z = Z_{axis}$ of the plbsma.

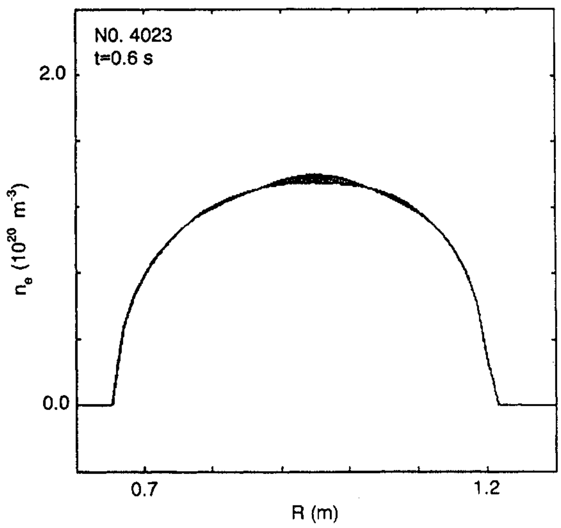

FIG. 35. Inverted electron density profile, on the symmetry plane $Z = Z_{axis}$ of the plasma, for shot No. 4023 at t = 0.6 s. The shaded region shows the uncertainty due to two different choices for the parametrization of $n_e(\psi)$, $n_0 + n_1\psi^{1/2} + n_2\psi + n_3\psi^{3/2}$ and $n_0 + n_1\psi^{1/2} + n_4\psi^{4/2} + n_5\psi^{5/2}$, respectively.

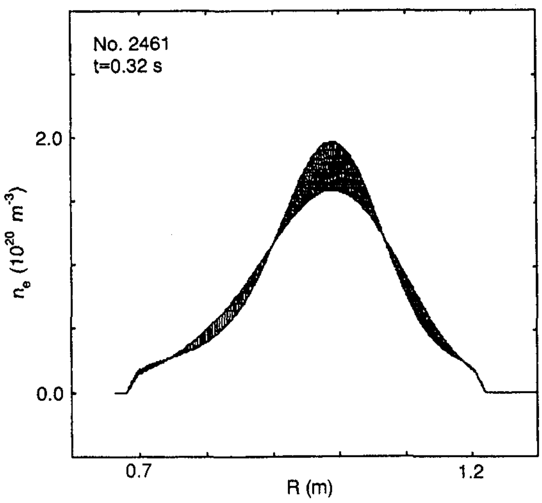

FIG. 36. Inverted electron density profile, on the symmetry plane $Z = Z_{axis}$ *of the plasma, for shot No. 2461 at* $t = 0.32$ *s, characterized by a plasma detachment phenomenon. The shaded regions show the uncertainty due to two different choices for the parametrization of* $n_e(\psi)$, $n_0 + n_1\psi^{1/2} + n_2\psi + n_3\psi^{3/2}$ *and* $n_0 + n_1\psi^{1/2} + n_4\psi^{4/2} + n_5\psi^{5/2}$, *respectively.*

angles of the measurement chords reduced to the unit Zernicke circle: $p_j = |R_j - R_{\rm axis}|/R_{\rm d}$, $\phi_j = 0$ if $R_j \geq R_{\rm axis}$, $\phi_j = \pi$ if $R_j < R_{\rm axis}$.

The system (11) is solved, by minimizing the sum of the squares of the mismatch of every equation, at first with $K = 2$; then the five measurement points are mirrored with respect to the magnetic axis, based on the result of the first inversion, and system (11) is finally solved for $j = 1, 18$ (5 DCN chords + 8 zero chords + 5 mirrored chords) with $K = 3$; this procedure will be referred to as the standard choice for

$$n_{\rm e}(\psi) = n_0 + n_1\psi^{1/2} + n_2\psi^{2/2} + n_3\psi^{3/2}$$

which is Eq. (4).

An example of the fit for the line integrated electron density is shown in Fig. 34 for shot No. 4023. The choice of using the lowest exponents in Eq. (7) after $\psi^{1/2}$ is arbitrary: in order to investigate a selection of higher exponents, inversions that use

$$n_{\rm e}(\psi) = n_0 + n_1\psi^{1/2} + n_4\psi^{4/2} + n_5\psi^{5/2}$$

have been performed (the non-standard choice). The inverted electron density profile is shown in Fig. 35 for shot No. 4023, both for the standard and for the non-standard choice for the exponents of $n_{\rm e}(\psi)$.

Whereas the low and medium q_ψ discharges have broad density profiles and very small uncertainties, the high q_ψ discharges exhibit more peaked density profiles and so larger uncertainties. The discharges characterized by a plasma detachment phenomenon, such as shot No. 2461, exhibit the most peaked density profiles and the uncertainty in the density inversion, due to the choice of the exponents, becomes rather large (see Fig. 36).

ACKNOWLEDGEMENTS

The authors would like to thank the entire FTU team. Particular acknowledgements are due to A. Cecchini, F. Crisanti, D. Fabiani, M. Gasparotto, A. Grosso, E. Lunadei, S. Mantovani, A. Marra, G.B. Righetti and S. Viselli for suggestions, discussions, designs and help during the construction and the assembly of the FTU equilibrium magnetic measurements. Acknowledgements for suggestions, discussions and help during the debugging of these measurements and their interfacing with the data acquisition and archive systems are due to R. Bartiromo, G. Buceti, G. Bracco, M. Marinucci, G.B. Righetti, J. Snipes and M. Zoffoli. Also P. Buratti, O. Tudisco and M. Zerbini, for the ECE measurements, and M. Grolli, for the DCN interferometer measurements, have to be thanked for providing the data of their diagnostics with a reliability without which this work would not have been possible. F. Crisanti has to be thanked for the common work with one of the authors of this paper in the development of the first version of the Zernicke density inversion code, which was developed and applied to the JET experiment in 1987. Finally, a particular acknowledgement is due to the team that has operated the FTU tokamak and that has produced all the plasmas investigated in this paper, i.e. to G. Apruzzese, F. Crisanti, D. Frigione, H. Kroegler, L. Lovisetto, G. Mazzitelli and S. Podda.

REFERENCES

[1] ALLADIO, F., CRISANTI, F., Nucl. Fusion **26** (1986) 1143.
[2] CHRISTIANSEN, J.P., TAYLOR, J.B., Nucl. Fusion **22** (1982) 111.
[3] LUXON, J.L., BROWN, B.B., Nucl. Fusion **22** (1982) 813.
[4] LAO, L.L., et al., Nucl. Fusion **25** (1985) 1421.
[5] LAO, L.L., et al., Nucl. Fusion **25** (1985) 1611.
[6] LAO, L.L., et al., Nucl. Fusion **30** (1990) 1035.
[7] POWELL, E.T., et al., Nucl. Fusion **33** (1993) 1493.
[8] SEGRE, S.E., Plasma Phys. **20** (1978) 295.
[9] SOLTWISCH, H., Rev. Sci. Instrum. **57** (1986) 1939.
[10] HOFMANN, F., TONETTI, G., Nucl. Fusion **28** (1988) 1871.

[11] JOFFRIN, E., et al., in Controlled Fusion and Plasma Physics (Proc. 20th Eur. Conf. Lisbon, 1993), Vol. 17C, Part I, European Physical Society, Geneva (1993) 107.
[12] LEVINTON, F.M., et al., Phys. Rev. Lett. **63** (1989) 2060.
[13] WRÓBLEWSKI, D., LAO, L.L., Phys. Fluids B **3** (1991) 2877.
[14] WRÓBLEWSKI, D., SNIDER, R.T., Phys. Rev. Lett. **71** (1993) 859.
[15] HIRSHMAN, S.P., et al., in Controlled Fusion and Plasma Physics (Proc. 20th Eur. Conf. Lisbon, 1993), Vol. 17C, Part III, European Physical Society, Geneva (1993) 1187.
[16] McCORMICK, K., et al., Phys. Rev. Lett. **58** (1987) 491.
[17] WEST, W.P., et al., Phys. Rev. Lett. **26** (1987) 2758.
[18] TERRY, J.L., et al., Rev. Sci. Instrum. **63** (1992) 5191.
[19] ANDREANI, R., et al., in Fusion Technology (Proc. 16th Symp. London, 1990), Vol. 1, Elsevier, Amsterdam and New York (1991) 218.
[20] SHAFRANOV, V.D., Sov. Phys.–JETP **6** (1958) 545.
[21] MORSE, P.M., FESHBACH, H., Methods of Theoretical Physics, McGraw-Hill, New York (1953).
[22] FOCK, V.A., Fiz. Zh. Sovietunion 1 (1932) 215.
[23] SHAFRANOV, V.D., Plasma Phys. **13** (1971) 757.
[24] BURATTI, P., et al., in Diagnostics for Contemporary Fusion Experiments (Proc. Course and Workshop, Varenna, 1991), Editrice Compositori, Bologna (1991) 787.
[25] GROLLI, M., ibid., p. 721.
[26] CORMACK, A.M., J. Appl. Phys. **34** (1963) 2722.
[27] NAGAYAMA, Y., et al., Jap. J. Appl. Phys. **20** (1981) 779.
[28] GRANETZ, R.S., SMEULDERS, P., Nucl. Fusion **28** (1988) 457.
[29] ALLADIO, F., et al., in Controlled Fusion and Plasma Physics (Proc. 18th Eur. Conf. Berlin, 1991), Vol. 15C, Part I, European Physical Society, Geneva (1991) 77.
[30] SNIPES, J.A., et al., Nucl. Fusion **30** (1990) 205.
[31] BOMBARDA, F., et al., in Controlled Fusion and Plasma Physics (Proc. 20th Eur. Conf. Lisbon, 1993), Vol. 17C, Part I, European Physical Society, Geneva (1993) 115.
[32] KADOMTSEV, B.B., Sov. J. Plasma Phys. **1** (1975) 389.
[33] PARAIL, V.V., PEREVERZEV, G.V., Sov. J. Plasma Phys. **6** (1980) 14.
[34] WESSON, J.A., Nucl. Fusion **30** (1990) 2545.
[35] TUDISCO, O., Rev. Sci. Instrum. **61** (1990) 2905.
[36] SPITZER, L., Jr., HÄRM, R., Phys. Rev. **89** (1953) 977.
[37] HIRSHMANN, S.P., et al., Nucl. Fusion **17** (1977) 611.
[38] ALLADIO, F., et al., Plasma Phys. Control. Fusion B **35** (1993) 241.
[39] ALLADIO, F., VLAD, G., Phys. Fluids **31** (1988) 602.
[40] WELLER, A., et al., Phys. Rev. Lett. **59** (1987) 2303.
[41] MIRNOV, S.V., SEMENOV, I.B., Sov. Phys.–JETP **33** (1971) 1134.
[42] FURTH, H.P., et al., Phys. Fluids **6** (1963) 459.
[43] WESSON, J.A., Nucl. Fusion **18** (1978) 87.
[44] WHITE, R.B., et al., Phys. Fluids **20** (1977) 800.
[45] ALLADIO, F., et al., in Controlled Fusion and Plasma Physics (Proc. 20th Eur. Conf. Lisbon, 1993), Vol. 17C, Part I, European Physical Society, Geneva (1993) 203.
[46] PIZZOLATI, P., et al., Rev. Sci. Instrum. **63** (1992) 4403.
[47] ANDREANI, R., et al., in Fusion Technology (Proc. 16th Symp. London, 1990), Vol. 2, Elsevier, Amsterdam and New York (1991) 1084.
[48] TFR GROUP, Nucl. Fusion **18** (1978) 647.
[49] HUTCHINSON, I.H., Lectures in Plasma Diagnostics, Rep. PFC/CP-90-1, MIT, Cambridge, MA (1990).
[50] HAKKARAINEN, S.P., FREIDBERG, J.P., Reconstruction of Vacuum Flux Surfaces from Diagnostic Measurements in a Tokamak, Rep. PFC/RR-87-22, MIT, Cambridge, MA (1987).

(Manuscript received 25 April 1994
Final manuscript received 28 September 1994)